The Journal of Immunology

RESEARCH ARTICLE | FEBRUARY 01 2018

The STAT3–IL-10–IL-6 Pathway Is a Novel Regulator of Macrophage Efferocytosis and Phenotypic Conversion in Sterile Liver Injury

Lara Campana; ... et. al

J Immunol (2018) 200 (3): 1169–1187.
https://doi.org/10.4049/jimmunol.1701247

The STAT3–IL-10–IL-6 Pathway Is a Novel Regulator of Macrophage Efferocytosis and Phenotypic Conversion in Sterile Liver Injury

Lara Campana,*,† Philip J. Starkey Lewis,† Antonella Pellicoro,* Rebecca L. Aucott,* Janet Man,† Eoghan O'Duibhir,† Sarah E. Mok,‡ Sofia Ferreira-Gonzalez,† Eilidh Livingstone,† Stephen N. Greenhalgh,* Katherine L. Hull,§ Timothy J. Kendall,*,¶ Douglas Vernimmen,‖ Neil C. Henderson,* Luke Boulter,# Christopher D. Gregory,* Yi Feng,* Stephen M. Anderton,* Stuart J. Forbes,*,† and John P. Iredale*,**

The disposal of apoptotic bodies by professional phagocytes is crucial to effective inflammation resolution. Our ability to improve the disposal of apoptotic bodies by professional phagocytes is impaired by a limited understanding of the molecular mechanisms that regulate the engulfment and digestion of the efferocytic cargo. Macrophages are professional phagocytes necessary for liver inflammation, fibrosis, and resolution, switching their phenotype from proinflammatory to restorative. Using sterile liver injury models, we show that the STAT3–IL-10–IL-6 axis is a positive regulator of macrophage efferocytosis, survival, and phenotypic conversion, directly linking debris engulfment to tissue repair. ***The Journal of Immunology*****, 2018, 200: 1169–1187.**

Phagocytosis is an evolutionarily conserved, multistep process that spans the recognition and engulfment of phagocytic cargo, through cargo processing to Ag presentation (1). Prompt removal of apoptotic and necrotic cells (efferocytosis) is critical to immune tolerance induction and maintenance or re-establishment of tissue homeostasis (2). A failure of efficient efferocytosis has been implicated in the pathogenesis of autoimmune and inflammatory disorders (3–5) such as systemic lupus erythematosus. Chronic inflammatory conditions are characterized by an aberrant release of proinflammatory intracellular components from secondary apoptotic and necrotic cells that fail to be cleared (6, 7). In solid tumors, recognition of apoptotic cells can promote an immunogenic response and antitumoral acquired immune responses (8). Efferocytosis has been postulated to be a mechanism through which initial organ damage, i.e., cell death, programs tissue remodeling, and regeneration. However, the molecular mechanisms underpinning this are not well understood (1, 9); understanding such mechanisms in this process could allow therapeutic targeting. Macrophages are professional phagocytes (10), and they change phenotype depending on microenvironmental cues, which include efferocytosis (11–13). We and others have previously characterized a hepatic restorative macrophage, derived from recruited inflammatory macrophages, which is necessary for tissue remod-

*Medical Research Council Centre for Inflammation Research, University of Edinburgh, Edinburgh EH16 4TJ, United Kingdom; †Medical Research Council Centre for Regenerative Medicine, University of Edinburgh, Edinburgh EH16 4UU, United Kingdom; ‡University of Edinburgh, Edinburgh EH16 4SB, United Kingdom; §University Hospitals of Leicester, Leicester LE3 9QP, United Kingdom; ¶Division of Pathology, University of Edinburgh, Edinburgh EH4 2XU, United Kingdom; ‖Developmental Biology Division, The Roslin Institute, University of Edinburgh, Edinburgh EH25 9RG, United Kingdom; #Medical Research Council Human Genetics Unit, Institute of Genetics and Molecular Medicine, University of Edinburgh, Edinburgh EH4 2XU, United Kingdom; and **Senate House, University of Bristol, Bristol BS8 1TH, United Kingdom

ORCIDs: 0000-0003-1805-4755 (L.C.); 0000-0002-3599-1567 (E.L.); 0000-0003-0028-5408 (K.L.H.); 0000-0002-4174-2786 (T.J.K.); 0000-0002-1308-9919 (D.V.); 0000-0002-7954-6705 (L.B.); 0000-0002-7553-0132 (C.D.G.); 0000-0001-8021-7776 (Y.F.).

Received for publication August 30, 2017. Accepted for publication November 25, 2017.

This work was supported by Medical Research Council Program Grant MR/J010766/1, Defining The Macrophage-Regulatory T Cell Axis That Promotes Fibrosis Resolution in the Liver (to primary investigator J.P.I. and coapplicants S.J.F. and S.M.A.); UK Regenerative Medicine Platform (UKRMP) Hub Grant MR/K026666/1, the Centre for the Computational and Chemical Biology of the Niche (to principal investigator S.J.F.); UKRMP Hub Grant MR/L012766/1, The Computational and Chemical Biology of the Stem Cell Niche (to principal investigator S.J.F.); Medical Research Council, Leverhulme Trust, and AMMF grants (to L.B.); Welcome Trust funding (to T.J.K.); and a Bloodwise research grant (to C.D.G.).

L.C. designed and performed the experiments, analyzed the data, and wrote the manuscript. P.J.S.L. performed experiments, helped in the design of the in vitro phagocytosis using live imaging, helped with the writing of the *Materials and Methods*, and with the revision of the manuscript. A.P. helped design the preliminary experiments, performed experiments, and helped with the setup of the image analysis for immunohistochemistry. S.F.-G., E.L., R.L.A., S.E.M., J.M., and K.L.H. performed experiments. S.N.G. helped with the animal work. T.J.K. acquired pictures with the multi-slide scanner from all the H&E sections and wrote the macro to analyze the necrotic area in acetaminophen-dosed mice. E.O. gave crucial support with the technical development and the analysis of the in vitro live imaging experiments. D.V. helped with the design of the experiment for NF-κB's role in phagocytosis and performed experiments. Y.F. helped in the design of the experiments with zebrafish, helped in performing experiments, provided a full *Materials and Methods* section for the zebrafish experiments, and revised the manuscript. L.B. helped in designing and performing gene analysis experiments, and revised the manuscript. C.D.G. and N.C.H. helped in designing experiments and revised the manuscript. S.M.A. wrote the project, helped define the experimental strategy, and provided support in data interpretation. S.J.F. and J.P.I. wrote the project, helped define the experimental strategy, provided support in data analysis and interpretation, and contributed to manuscript preparation, editing, and revision.

Address correspondence and reprint requests to Dr. Lara Campana, University of Edinburgh, 5 Little France Drive, Edinburgh EH16 4UU, U.K. E-mail address: Lara.Campana@ed.ac.uk

The online version of this article contains supplemental material.

Abbreviations used in this article: ALP, alkaline phosphatase; ALT, alanine aminotransferase; APAP, acetaminophen; apoT, apoptotic thymocyte; AST, aspartate aminotransferase; BMDM, bone marrow–derived macrophage; CCl_4, carbon tetrachloride; CT, cycle threshold; Gpnmb, glycoprotein nonmetastatic melanoma B; HCC, hepatocellular carcinoma; hMDM, human monocyte–derived macrophage; KO, knockout; LC3, L chain 3; NPC, nonparenchymal cell; p, plasma; pSTAT3, phosphoSTAT3; qPCR, quantitative PCR; rm, recombinant murine; WT, wild-type.

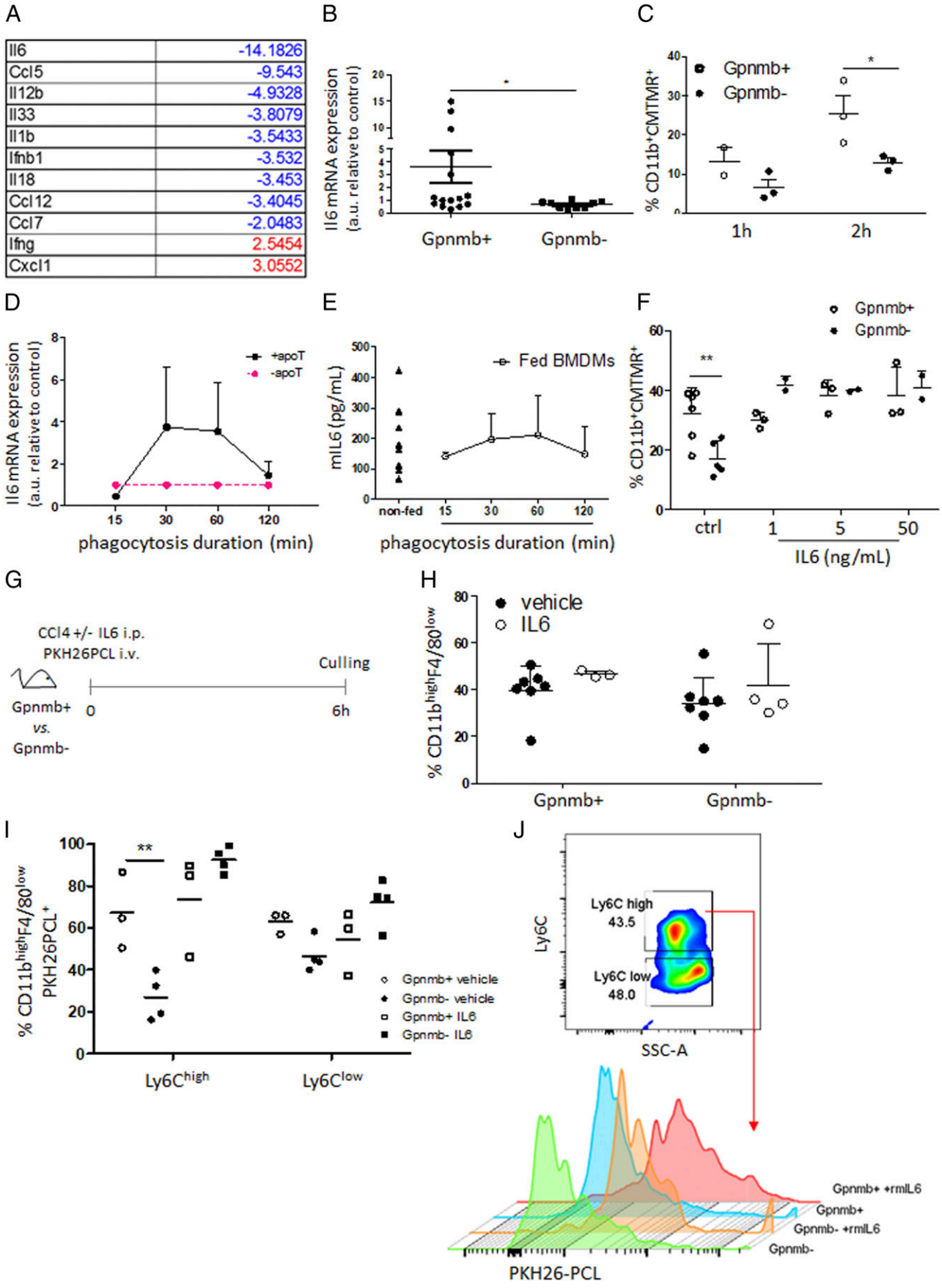

FIGURE 1. IL-6 treatment rescues the phenotype of macrophages deficient for phagocytic cargo digestion in vitro and in vivo. (**A**) Low-density qPCR array analysis has been performed on mRNA extracted from Gpnmb$^+$ and Gpnmb$^-$ BMDMs fed with apoTs overnight (o.n., $n = 3$). Data are expressed as relative expression of the average of the expression of each gene in the sample group (Gpnmb$^-$) versus control group (Gpnmb$^+$). A representative list of the most regulated genes is reported. In blue are the most downregulated genes, in red the genes upregulated of >2 *(Figure legend continues)*

eling and regeneration following sterile liver injury (14, 15). Furthermore, in liver injury, phagocytosis of necrotic hepatocytes by macrophages prompts Wnt ligand secretion, which promotes liver regeneration (16).

In this study, we have derived macrophages from the bone marrow of control (glycoprotein nonmetastatic melanoma B, Gpnmb$^+$) mice or of mice that have a defect in Gpnmb (Gpnmb$^-$), an interactor of L chain 3 (LC3). Gpnmb$^-$ macrophages will engulf but fail to process their apoptotic cell cargo (17, 18). Macrophages have been fed with apoTs to study the activation of intracellular pathways downstream from the engulfment and digestion of phagocytic cargo. We show that macrophage phosphoSTAT3 (pSTAT3) is a prophagocytic mediator that enhances macrophage phagocytosis, via rapid nontranscriptional regulation of IL-10. pSTAT3 activation is sustained at the later stages of phagocytosis, promoting IL-6 transcription and thereby making efferocytosis more efficient. Following acute and chronic sterile liver injury, Gpnmb$^-$ mice exhibited extensive liver damage and increased numbers of proinflammatory macrophages. Treatment with recombinant IL-6 is sufficient to increase efferocytosis in vivo and to promote macrophage phenotypic conversion to prorestorative macrophages.

Materials and Methods

Mice

C57BL/6 mice (CD45.2$^+$) were purchased from Charles River U.K. C57BL/6 IL-6 knockout (KO) mice (19) were provided by Prof. S. Anderton, University of Edinburgh. Gpnmb$^+$ (DBA/2J-Gpnmb$^+$/SjJ) and Gpnmb$^-$ (DBA2J) mice were originally imported from the Jackson Laboratory (17). The colony was propagated at the University of Edinburgh. Mice were housed in groups of five or six in open-top cages, and synchronized to a 10–14 h dark/light cycle with access to food and water ad libitum. Mice were bred under specific pathogen-free conditions at the University of Edinburgh. All experiments had local ethical approval and were conducted under U.K. Home Office legislation. Genotyping was carried out by using PCR by TransnetYX.

Liver fibrosis model

Wild-type (WT) C57BL6 male mice were allowed to acclimatize for a minimum of 1 wk in a clean animal facility. Prior to carbon tetrachloride (CCl_4) treatment, mice were randomly assigned to treatment groups. Adult male mice (10–12 wk old) were used. Hepatic fibrosis was induced by two injections per week of CCl_4 (0.4 μl/g; Sigma-Aldrich) i.p., diluted 1:3 in olive oil (Sigma-Aldrich) for 6 wk. Animals were culled at stated time points after the final CCl_4 injection.

Acetaminophen-induced liver injury and bone marrow–derived macrophage administration

WT C57BL6 male mice (10 wk old) were allowed to acclimatize for a minimum of 1 wk in a clean animal facility. Prior to acetaminophen (APAP) administration, mice were fasted for at least 12 h. Mice received a single injection (i.p.) of APAP (300 mg/kg) dissolved in warm saline between 23:00 and midnight. Mice were left to recover until morning on a heated mat or in a warm rack; at indicated time points, they were humanely culled according to local ethical guidelines.

Acute liver damage by single injection of CCl4

Adult male mice at least 8 wk old were used. Acute liver injury was induced by i.p. injection of CCl_4 (0.4 μl/g; Sigma-Aldrich) diluted 1:3 in olive oil (Sigma-Aldrich). Animals were culled at stated time points after CCl_4 injection.

Phagocytosis assay in vivo

Mice dosed with APAP or receiving a single CCl_4 injection were injected with 100 μl 0.1 mM PKH26PCL diluted 1:10 according to the manufacturer's instructions (Sigma-Aldrich, U.K.) i.v. via the tail vein to label phagocytic cells. Control mice were injected with 100 μl of diluent only. The percentage of phagocytic cells in hepatic infiltrating and resident is reported. Mice were culled 6 h post-CCl_4 and livers were harvested and processed as described for flow cytometry analysis. Numbers were calculated based on the cell counting performed after isolation of the nonparenchymal cell (NPC) fraction. The percentage of phagocytic cells was calculated on the gate of viable CD45$^+$Ly6G$^-$CD3$^-$CD19$^-$NK1.1$^-$ cells.

Bone marrow–derived macrophage adoptive transfer

We transferred Gpnmb$^+$ CFSE-labeled bone marrow–derived macrophages (BMDMs) and Gpnmb$^-$ CMTMR-labeled BMDMs into C57BL/6 mice receiving a single dose of CCl_4. Mice received either Gpnmb$^+$ or Gpnmb$^-$ BMDMs or both populations in a 1:1 ratio. To avoid an effect of the labeling on the parameter analyzed, the experiment was repeated using Gpnmb$^+$ CMTMR-labeled BMDMs and Gpnmb$^-$ CFSE-labeled BMDMs. CFSE-labeled or CMTMR-labeled BMDMs were resuspended in Dulbecco's PBS and administered (2.5×10^6 cells, 100 μl) via the tail vein to mice under gaseous isoflurane/oxygen anesthesia at 2 h after the single CCl_4 injection. Mice were humanely culled by asphyxiation in a rising CO_2 atmosphere. Death was confirmed by neck dislocation. CFSE-labeled or CMTMR-labeled BMDMs were injected 2 h after CCl_4 dosing. CFSE- and CMTMR-labeling efficiency was routinely >90%. Viability post-transfer was routinely >90%. Mice were culled 6 h post-CCl_4 and livers were harvested and processed as described for flow cytometry analysis.

Transferred BMDMs were identified as CFSE$^+$ or CMTMR$^+$. The percentage of CFSE$^+$/CMTMR$^+$ cells was calculated on the gate of total viable CD45$^+$Ly6G$^-$CD3$^-$CD19$^-$NK1.1$^-$ cells. The negative was set on a liver from a nontransplanted mouse. The percentage of Ly6C$^+$ and Ly6C$^-$ was calculated on the gate of CFSE$^+$/CMTMR$^+$ cells. The negative was set using the liver from a nontransplanted animal (for single CFSE$^+$ and

fold in the sample versus control group. The full list of genes analyzed is provided in Supplemental Fig. 1. (**B**) Il-6 mRNA analysis on RNA from BMDMs fed with apoTs at a phagocyte/target ratio of 1:5 o.n. Gene expression has been calculated using the ΔΔCT method relative to housekeeping gene β-actin. The graph reports the ratio between the ΔΔCT of the fed cells with the ΔΔCT of one of the control, untreated Gpnmb$^+$ BMDMs. Data have been analyzed with Student *t* test for unpaired data. $*p < 0.05$. (**C**) Percentage of phagocytic Gpnmb$^+$ (white dots) and Gpnmb$^-$ (black dots) BMDMs fed with CMTMR-labeled apoTs. Each dot represents a biological replicate. (**D**) Il-6 mRNA dosage on RNA from BMDMs fed with apoT at a phagocyte/target ratio of 1:5 for the indicated time point (black solid line) or not fed with apoT (pink dotted line). Gene expression has been calculated using the ΔΔCT method relative to housekeeping gene β-actin. The graph reports the ratio between the ΔΔCT of each time point with the ΔΔCT of one of the control, untreated BMDMs at the same time point. (**E**) IL-6 protein has been analyzed in the supernatant of the same BMDMs at the indicated time points. Results are expressed as picograms per milliliter. Average ± SD of three independent experiments is reported. Unfed BMDMs: each triangle equals a supernatant from one well of unfed macrophages. Results of three independent experiments are pulled. (**F**) Percentage of phagocytic Gpnmb$^+$ (white dots) and Gpnmb$^-$ (black dots) BMDMs fed with CMTMR-labeled apoTs in the presence or absence of rmIL-6 at the indicated concentration for 120 min. Each dot represents a biological replicate. (**G**) Experimental design: Gpnmb$^+$ and Gpnmb$^-$ mice have been injected i.p. with a single CCl_4 injection and with rmIL-6 or saline. PKH26PCL has been injected at the time of damage via tail vein to track phagocytic cell in vivo. Mice are culled after 6 h and liver is harvested, digested, and labeled for flow cytometry analysis. (**H**) Flow cytometry analysis of liver digest. Infiltrating macrophages have been identified as described in Supplemental Fig. 1. Each dot represents the analysis of one liver digest. Black dots = vehicle (PBS)-treated mice. Empty dots = rmIL-6–treated mice (**I** and **J**). Flow cytometry analysis of liver digest. The percentage of phagocytic macrophages is calculated as percentage of PKH26PCL$^+$ events in the gate of Ly6C^{high} and Ly6C^{low} events [representative density plot and histograms in (J)]. (I) White dots: Gpnmb$^+$ mice treated with CCl_4 and vehicle (PBS). Black dots: Gpnmb$^-$ mice treated with CCl_4 and vehicle. White square; Gpnmb$^+$ mice treated with CCl_4 and rmIL-6. Black square: Gpnmb$^-$ mice treated with CCl_4 and rmIL-6. Each dot is a distinct mouse. Mean is reported. (D–F, H, and I) Data have been analyzed with one-way or two-way ANOVA for unpaired data when appropriate followed by a Bonferroni posthoc test to compare all pairs of columns. Data have been checked for equal variance before further analysis. $*p < 0.05$, $**p < 0.01$.

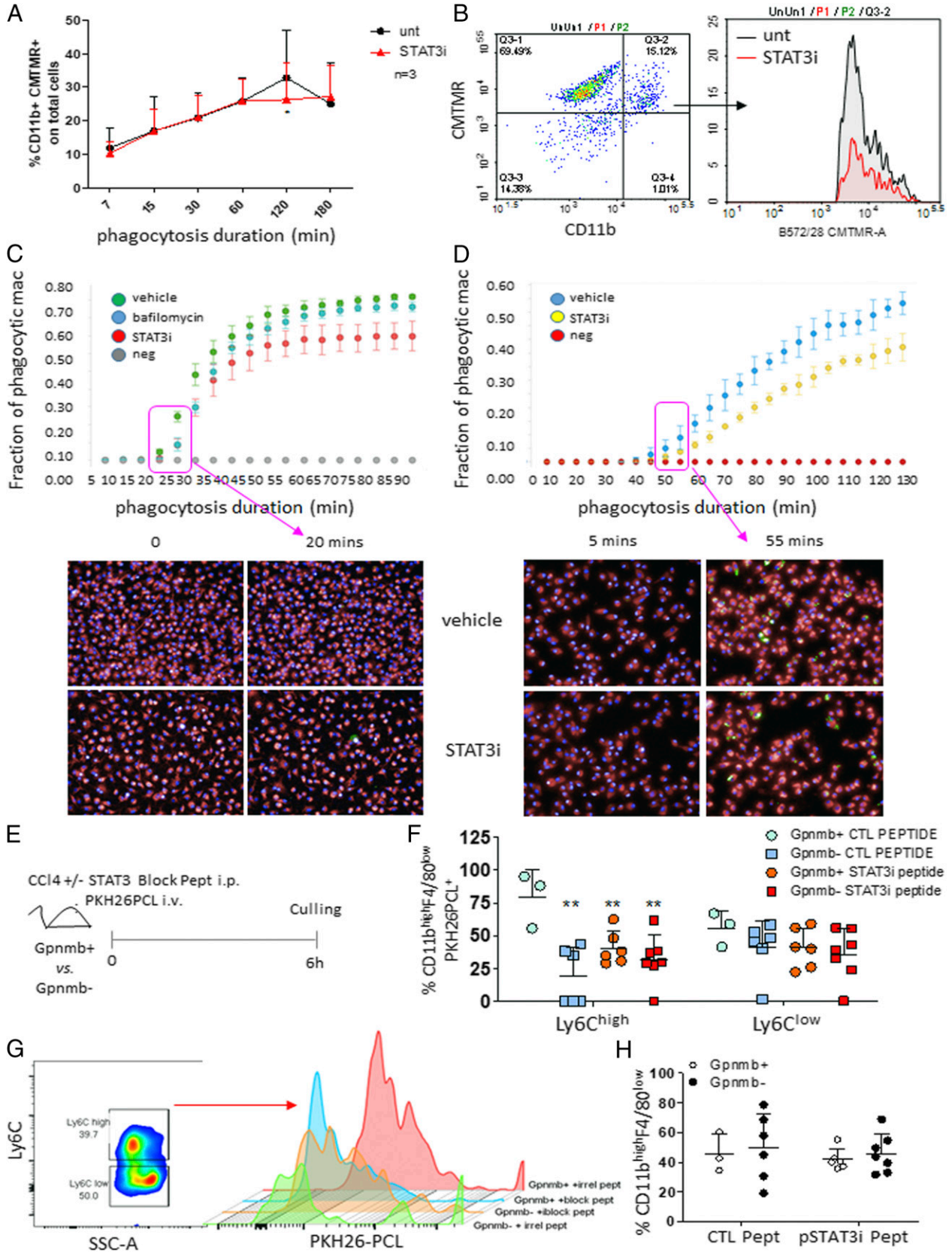

FIGURE 2. pSTAT3 is upstream IL-6 effect in the control efferocytosis. (**A**) BMDMs fed with CMTMR-labeled apoT in the presence of vehicle (DMSO) or pSTAT3 (Tyr506) inhibitory peptide at various time points after adding apoT. $n = 3$, average ± SD is reported. Data have been analyzed with two-way ANOVA for unpaired data followed by Bonferroni posthoc test to compare all pairs of columns. Data have been checked for equal variance before further analysis. $*p < 0.05$, $**p < 0.01$. (**B**) Representative dot plot and histogram plot for the analysis carried out in (A). (**C**) Live imaging of BMDMs phagocytosing pH-sensitive (pHrodo) beads. Results are expressed as proportion of phagocytic cells on total number of cells. Mean and SD at the indicated time points are reported for the distinct treatment groups. Green dots: BMDMs; blue dots: BMDMs+bafilomycin; red dots: BMDMs+pSTAT3 inhibitory peptide. In the bottom panel representative pictures from the live imaging are reported. (**D**) Live imaging of phagocytic *(Figure legend continues)*

CMTMR$^+$) or transplanted with BMDMs labeled with the other tracker (CFSE for CMTMR and vice versa).

Sample isolation and storage

Whole blood was collected via cardiac puncture or from the inferior vena cava using 30 μl heparin (200 U/ml) per sample. Blood was centrifuged at 10,000 rpm for 10 s at room temperature in a bench centrifuge (Eppendorf), and plasma was isolated and snap-frozen using dry ice. Plasma was then stored at −80°C and used for protein dosages. Liver tissue was harvested and the left lateral lobe was separated into two pieces and placed in either a freezing isopentane bath or fixed in methacarn for 24 h. The remaining liver and other organs were fixed in formalin (4% paraformaldehyde) for 24 h before paraffin embedding. The central lobe was used for isolation of hepatic NPCs and flow cytometry analysis.

Isolation of hepatic NPCs

Isolation of the hepatic NPC fraction was performed as described previously (16, 20) with minor modifications. Briefly, mouse livers in situ were perfused with 5 ml 0.9% NaCl solution through the inferior vena cava followed by cutting of the portal vein to remove circulating cells. Livers were then harvested and weighed; the right lobe was homogenized using a scalpel and digested in RPMI 1640 containing collagenase V (0.8 mg/ml; Sigma-Aldrich), collagenase D (0.625 mg/ml; Roche), dispase (1 mg/ml; Life Technologies), collagenase D (1.6 mg/ml; Roche), and DNase I (100 μg/ml; Roche) for 25 min at 37°C, shaking vigorously every 5 min. Digested livers were passed through 70 μm cell strainers, and enzymes were inactivated by the addition of RPMI 1640 with 10% FCS. The NPC fraction containing hepatic macrophages was harvested by two centrifugations at 300 × *g*, 4°C, 5 s, followed by red cell lysis with 3 ml 1× lysis buffer (BD Pharm Lyse; BD Biosciences) for 5 min on ice. Cells were then counted, and used for flow cytometry.

NPC labeling and flow cytometry analysis

Nonspecific Ab binding was blocked by incubating cells with 10% mouse serum for 20 s at 4°C, followed by incubation with combinations of primary Abs (each used at 1:200 dilution) for 20 s at 4°C. The following conjugated Abs were used: CD11b BV650 (clone M1/70; eBioscience), Ly-6C V450 (clone HK1.4; eBioscience), CD45.2 AF700 (clone 104; eBioscience), F4/80 APC (dilution 1:100; clone BM8; Invitrogen), Ly-6G PE-Cy7 (clone 1A8; BioLegend), CD3 PE-Cy7 (clone 17A2; BioLegend), NK1.1 PE-Cy7 (clone PK136; BioLegend), CD19 PE-Cy7 (clone 6D5; BioLegend). Cell viability was assessed with Fixable Viability Dye eFluor780 (1:1000; eBioscience) according to the manufacturer's protocols. After Ab staining, samples were either analyzed immediately or fixed with 10% buffered formalin. Data were analyzed using FlowJo10 software (Tree Star). Hepatic RESIDENT macrophages were defined as viable CD45$^+$Ly-6G$^-$CD3$^-$NK1.1$^-$CD19$^-$CD11b^{low} F4/80^{high}. Hepatic infiltrating macrophages were defined as: viable, CD45$^+$ Ly6G$^-$CD3$^-$NK1.1$^-$CD19$^-$CD11b^{high}F4/80^{low} cells from NPC fraction of digested livers and used to identify macrophage subsets. Subsets were expressed as proportions of total hepatic macrophages or CD45$^+$ cells. Quantification of absolute numbers of cells per liver was performed by expressing each subset as a proportion of NPCs, counting total number of NPCs in the digested portion of liver, calculating the total number of NPCs in the whole liver by weight differential, and thus, calculating the total number of each subset. Circulating monocytes (from whole blood diluted 1:1 in heparin) were stained using BD Pharm Lyse (BD Biosciences) before analysis. Monocytes were identified as CD45$^+$CD11B$^+$Ly-6G$^-$CD3$^-$Ly-6C^{high} and Ly-6C^{low} cells from whole blood and expressed as a percentage of total peripheral mononuclear cells.

Plasma chemistry evaluation

Plasma chemistry was performed by measurement of alanine aminotransferase (ALT), aspartate aminotransferase (AST), alkaline phosphatase (ALP), total bilirubin, and plasma (p) albumin. ALT was measured using the method described previously (21), utilizing a commercial kit (Alpha Laboratories). AST and ALP were determined by a commercial kit (Randox Laboratories). Total bilirubin was determined by the acid diazo method described by Pearlman and Lee (22) using a commercial kit (Alpha Laboratories). Mouse plasma albumin measurements were determined using a commercial serum albumin kit (Alpha Laboratories). All kits were adapted for use on a Cobas Fara centrifugal analyzer (Roche Diagnostics). For all assays, intrarun precision coefficient of variation was <4%.

Phagocytosis assay in vitro—flow cytometry

BMDMs were prepared as described (14, 23) from adult male C57BL/6 mice. Briefly, we differentiated whole bone marrow for 7 d at 37°C, 5% CO_2 in DMEM/F12+Glutamax (Life Technologies) medium with 10% FCS and 25 μg/ml recombinant murine (rm) M-CSF (Miltenyi Biotec) under nonadherent conditions using Ultra-Low attachment flasks (Corning). This process routinely yielded a macrophage population of >90% purity as assessed by flow cytometry for CD11b. ApoTs were prepared as previously described (24). Briefly, thymuses were removed from C57BL/6 mice, aged 3–5 wk, homogenized in RPMI 1640 medium, and incubated with hydrocortisone (1 μM; Sigma-Aldrich) and 1% FCS at 37°C, 5% CO_2 for 16 h. This process routinely yielded a population of dead thymocytes with over 80% trypan blue positive. ApoTs were labeled using CMTMR (Invitrogen) as described previously (25). Briefly, macrophages were challenged with apoptotic cells for 7, 15, 30 min, 1 and 2 h at a 1:5 ratio at 37 or 4°C. Cells were washed and phagocytosis verified by flow cytometry after staining with anti-CD11b BV650 (clone M1/70; eBioscience) and anti–Ly-6C V450 (clone HK1.4; eBioscience). When the assay was performed in a 96-well plate (Ultra-Low attachment; Corning Costar) cytochalasin D 10 μM (Sigma-Aldrich) was used as a negative control. The phagocytosis was calculated as percentage of CD11b$^+$CMTMR$^+$ cells at 37°C minus the percentage of CD11b$^+$CMTMR$^+$ cells at 4°C. The percentage of Ly6C$^+$ cells was calculated in the gate of CD11b$^+$CMTMR$^+$ cells at 37°C. Mean fluorescence intensity for CMTMR was calculated on the same gate in the same conditions. Data were acquired on an LSRII Fortessa (BD Biosciences) when the assay was performed in tubes. Data were acquired and analyzed on a NovoCyte 3000 (Acea Biosciences) when the assay was performed on a 96 well-plate.

Phagocytosis assay in vitro—live imaging (Operetta, PerkinElmer)

BMDMs were plated (1×10^5 per well) in 96-well CellCarrier microplates (PerkinElmer) overnight before stimulation with appropriate cytokines or blockers (see *Materials and Methods*). Before imaging, BMDMs were stained with NucBlue live cell stain (Thermo Fisher Scientific) and CellMask Deep Red (Thermo Fisher Scientific) plasma membrane stain according to the manufacturer's instructions. Plates were transferred to Operetta high-content imaging system (PerkinElmer) and allowed to equilibrate at 37°C and 5% CO_2. Phagocytosis was initiated by the addition of pHrodo green zymosan bioparticles (Thermo Fisher Scientific) to the wells. Fluorescent images were taken in the DAPI channel, 488, and 647

hMDMs: results are expressed as a proportion of phagocytic cells on total number of cells. Mean and SD are reported. Red dots: negative control, unfed cells; blue dots: hMDMs treated with vehicle; yellow dots: hMDMs treated with pSTAT3 inhibitor. In the bottom panel representative pictures from the live imaging are reported. (**E**) Experimental design: Gpnmb$^+$ and Gpnmb$^-$ mice have been injected i.p. with CCl_4 once together with a pSTAT3 (Tyr506) blocking peptide or an irrelevant peptide. PKH26PCL has been injected at the time of damage via tail vein to track phagocytic cells. Mice are culled after 6 h and liver is harvested, digested, and labeled for flow cytometry analysis. (**F** and **G**) Flow cytometry analysis of liver digest. Infiltrating macrophages have been identified as described in Supplemental Fig. 1 and the percentage of phagocytic macrophages is calculated as the percentage of PKH26PCL$^+$ events in the gate of inflammatory (Ly6C^{high}) and restorative (Ly6C^{low}) macrophages. Light blue dots: Gpnmb$^+$ mice treated with CCl_4 and irrelevant peptide. Blue squares: Gpnmb$^-$ mice treated with CCl_4 and irrelevant peptide. Orange dots: Gpnmb$^+$ mice treated with CCl_4 and pSTAT3 blocking peptide. Red squares: Gpnmb$^-$ mice treated with CCl_4 and pSTAT3 blocking peptide. Each dot is a distinct mouse. Mean and SD are reported. (G) Representative histogram plot of PKH26PCL fluorescence in the gate of infiltrating inflammatory macrophages from livers of Gpnmb$^+$ (left panel) and Gpnmb$^-$ (right panel) mice. (**H**) Flow cytometry analysis of liver digest. Infiltrating macrophages have been identified as described in Supplemental Fig. 1. Each dot represents the analysis of one liver digest. White dots = Gpnmb$^+$. Black dots = Gpnmb$^-$. (F and H) Data have been analyzed with two-way ANOVA for unpaired data followed by a Bonferroni posthoc test to compare all pairs of columns. The distribution of the data has been checked for equal variance before applying any statistical test. *$p < 0.05$, **$p < 0.01$.

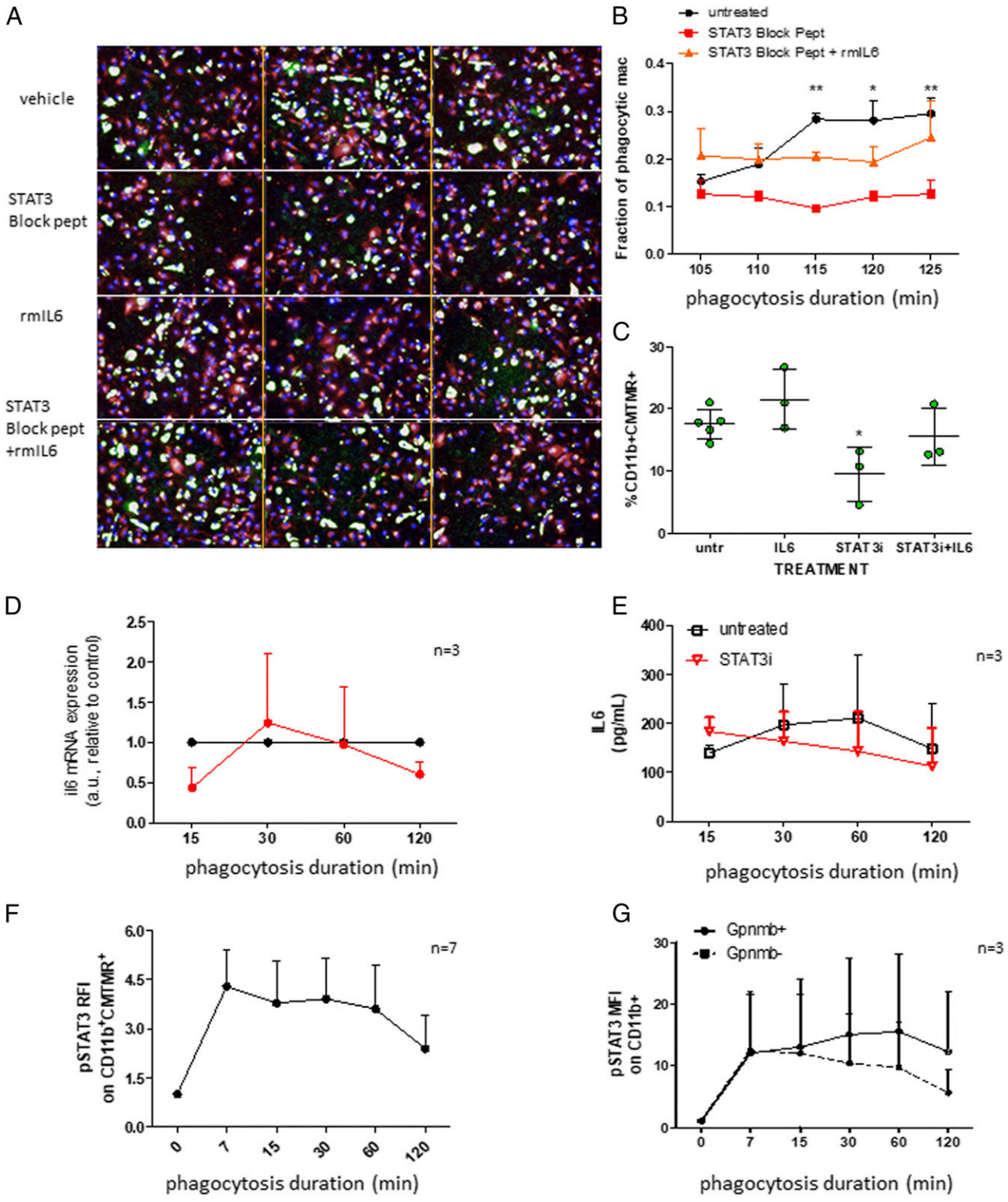

FIGURE 3. STAT3 phosphorylation is required for the maintenance of efficient efferocytosis. (**A**) Representative pictures from the live imaging are reported. Each picture is an independent well. Red = macrophage cytoplasm; blue = nucleus; green = phagocytosed zymosan A–coated beads. (**B**) Live imaging of BMDMs phagocytosing pH-sensitive (pHrodo) beads. Average ± SD at the distinct time points are reported for the distinct treatment groups. Black dots: untreated BMDMs; red dots: BMDMs+pSTAT3 inhibitory peptide; orange dots: BMDMs+pSTAT3 inhibitory peptide+rmIL-6. (**C**) Flow cytometry analysis of phagocytosis in untreated versus rmIL-6 50 ng/ml, pSTAT3(Y705) blocking peptide (STAT3i) 30 μM, or rmIL-6 50 ng/ml and pSTAT3(Y705) blocking peptide (STAT3i) 30 μM treated BMDMs. (**D**) Il-6 mRNA analysis on RNA from BMDMs fed with apoT and treated with the pSTAT3 inhibitory peptide at the indicated time points (solid red line) or treated with the vehicle (solid black line). Gene expression has been calculated using the ΔΔCT method relative to housekeeping gene 18s. The graph reports the ratio between the ΔΔCT of each time point with the ΔΔCT of one of the control, untreated BMDMs at the same time point. (**E**) IL-6 protein has been analyzed in the supernatant of the same BMDMs using a multiplex platform at the indicated time points. Results are expressed as picograms per milliliter. Average ± SD of three independent experiments is reported. (**F**) pSTAT3 expression after phagocytosis of apoT at distinct time points is analyzed by flow cytometry; the average ± SD of the relative fluorescence intensity is plotted. Relative fluorescence intensity is calculated as mean fluorescence intensity (MFI) of the sample divided by the MFI of the control (nonphagocytic naive BMDMs). (**G**) pSTAT3 expression after phagocytosis of apoT at distinct time points is analyzed by flow cytometry in Gpnmb$^+$ and Gpnmb$^-$ BMDMs; the mean and SD of the relative fluorescence intensity is plotted. Relative fluorescence intensity is calculated as MFI of the sample divided by the MFI of the control (non-phagocytic Gpnmb$^+$ and Gpnmb$^-$ BMDMs respectively). *$p < 0.05$, **$p < 0.01$, ***$p < 0.001$.

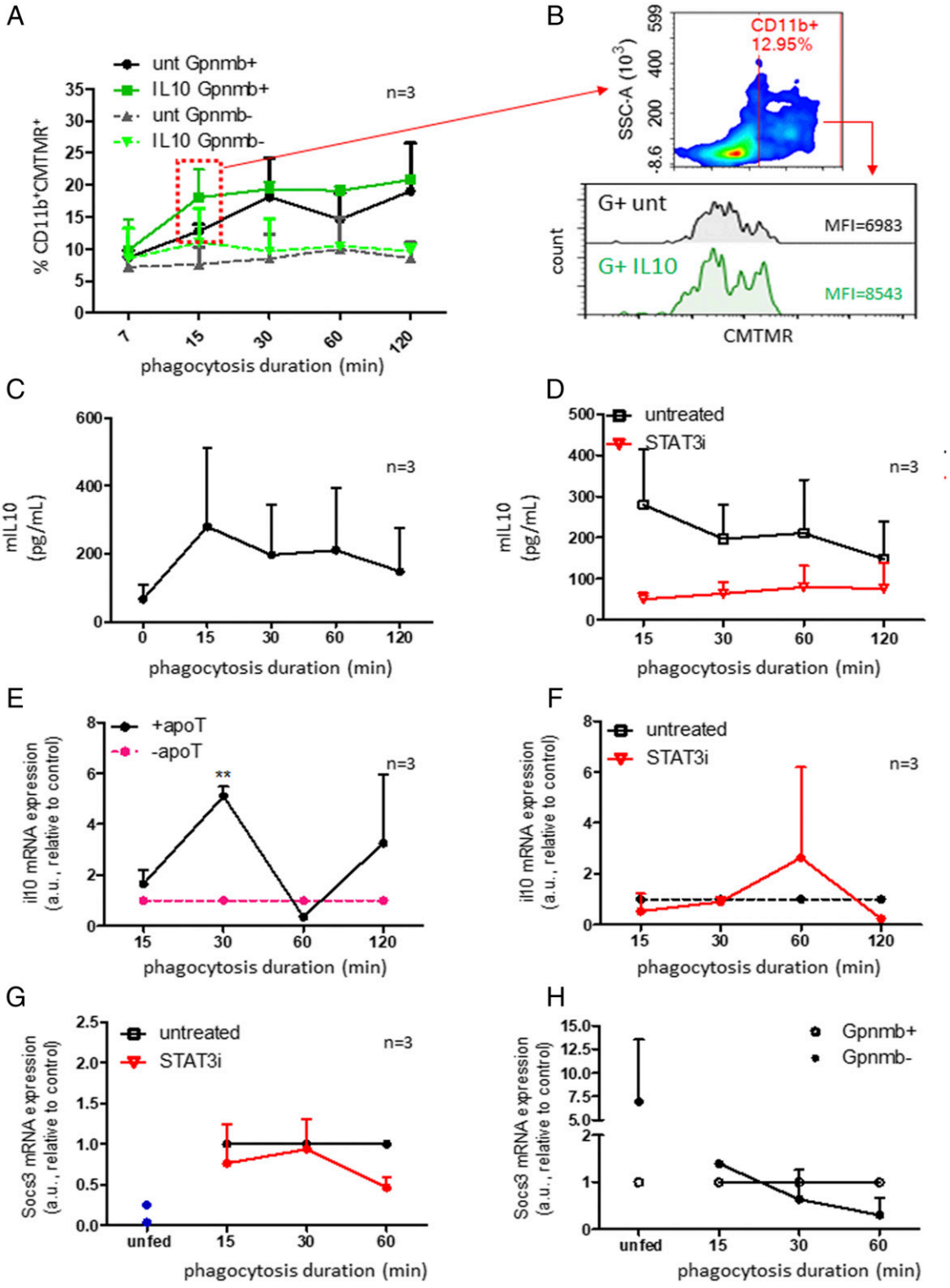

FIGURE 4. pSTAT3 drives IL-10 secretion early after the start of phagocytosis. (**A**) Gpnmb$^+$ (solid lines) and Gpnmb$^-$ (dotted lines) BMDMs fed with CMTMR-labeled apoT in the presence of vehicle (DMSO, black and gray lines) or rmIL-10 (green lines) at various time points after adding apoT. $n = 3$, average ± SD is reported. (**B**) Representative plots of CMTMR mean fluorescence intensity analyzed in Gpnmb$^+$ BMDMs (CD11b$^+$) treated or not with rmIL-10 at 15 s of efferocytosis (red dotted box in A). Further plots are reported in Supplemental Fig. 4A. (**C**) IL-10 protein has been analyzed in the supernatants of the same BMDMs at the indicated time points. Results are expressed as picograms per milliliter. Average ± SD of three independent experiments is reported. (**D**) IL-10 protein has been analyzed in the supernatants of the same BMDMs treated or not with the pSTAT3 blocking peptide (STAT3i) at the indicated time points. Results are expressed as picograms per milliliter. Average ± SD of three independent experiments is reported. (**E**) Il-10 mRNA dosage on RNA from BMDMs fed with apoT at a phagocyte/target ratio of 1:5 for the indicated time point (black solid line) or not fed with apoT (pink dotted line). Gene expression has been calculated using the ΔΔCT method relative to housekeeping gene β-actin. (**F**) Il-10 mRNA dosage on RNA from BMDMs fed with apoT and treated with the pSTAT3 inhibitory peptide (STAT3i) at the indicated time points (red solid line) or treated with the vehicle (black dotted line). Gene expression has been calculated using the ΔΔCT method relative to housekeeping gene 18s. (**G**) Socs3 mRNA dosage on RNA from BMDMs fed with apoT and treated with the pSTAT3 inhibitory peptide (STAT3i) at the indicated time *(Figure legend continues)*

nm before, and at 5 min intervals after the addition of bioparticles for a maximum of 150 min. Images were quantified on Columbus image analysis software (PerkinElmer). Macrophages positive for phagocytosis were classified based on a fluorescence intensity (488 nm) >500 and expressed as a fraction of all live cells (NucBlue-positive cells). Mean fraction values were taken from four separate wells per group.

Study of the pSTAT3–IL-10–IL-6 pathway

The role of pSTAT3–IL-10–IL-6 pathway in phagocytosis was investigated in vitro in the presence or absence of rmIL-6 (Miltenyi Biotec) at distinct concentrations: 1, 5, and 50 μg/ml. A pSTAT3 (Tyr705) inhibitory peptide or an irrelevant peptide (Merck Millipore) were used at a 30 μM final concentration in vitro. rmIL-10 was used at a final concentration of 10 ng/ml (Miltenyi Biotec) (25). For the Operetta live imaging experiment, BMDMs were treated with pSTAT3 inhibitory peptide either 2 h before the phagocytosis or during the phagocytosis itself.

For immunofluorescence of pSTAT3, BMDMs were fixed at distinct time points after the start of phagocytosis using PFA 4% for 15 min. Permeabilization was performed using TritonX100 (Sigma-Aldrich) for 15 min. To minimize nonspecific binding, we added protein block solution (SpringBio) for 30 min. Primary Abs used were: Phospho-Stat3 (Tyr705) (clone D3A7) XP rabbit mAb #9145 1 μg/ml (Cell Signaling Technology); GPNMB (K-16) goat pAb #Sc-47006 1 μg/ml (Santa-Cruz). Primary Abs were incubated for 3 h at room temperature. Secondary Abs were AlexaFluor488 and AlexaFluor555, respectively. Secondary Abs were incubated in the dark for 1 h at room temperature. BMDMs were then mounted on a slide using an aqueous mounting medium (Fluoromount-G; SouthernBiotech) and imaged using a Leica SP5 confocal microscope. AlexaFluor488 and 555 were detected using band paths of 495–540 and 561–682 nm for 488 and 543 nm lasers respectively.

The role of pSTAT3–IL-6 pathways in phagocytosis was investigated in vivo by injecting 50 μg per mouse of rmIL-6 (Miltenyi Biotec) i.p. IL-6 was injected together with CCl_4 in the single CCl_4 acute liver damage model. IL-6 was injected either with or 2 h after the administration of APAP. In the chronic model of CCl_4 intoxication IL-6 is injected at the same time of CCl_4 suspension to investigate the effect on the macrophage phenotype in $Gpnmb^+$ and $Gpnmb^-$ mice. A STAT3 inhibitory peptide or an irrelevant peptide (Merck Millipore) were used at a 30 μM final concentration following the same treatment regimen in the acute damage model by single CCl_4 injection and in the model of APAP intoxication.

RNA isolation and quantitative PCR

For whole liver, the caudate lobe was snap-frozen in liquid nitrogen and stored at −80°C. RNA was extracted using QIAshredder columns and RNeasy mini columns (Qiagen) according to the manufacturer's protocol, followed by quantification using the Nanodrop Spectrophotometer (Thermo Fisher Scientific); 0.5 μg RNA was reverse transcribed using SuperScript III (Invitrogen) according to the manufacturer's protocol. Gene expression was calculated using the ΔΔ cycle threshold (CT) method relative to housekeeping gene β-actin and Gapdh. For the in vitro phagocytosis assay, RNA was extracted using the QIAshredder columns and RNeasy mini columns (Qiagen), and 100 ng RNA were reverse transcribed using QuantiTect Reverse Transcription Kit (Qiagen) according to the manufacturer's protocol. cDNA was then diluted to 1:10 with RNase Free water, prior to quantitative PCR (qPCR) analysis. The following QuantiTect Primer Assays (Qiagen) were purchased: Tgf-β, Il-10, Il-10, Il-6, Hmgb1, Sdf1/Cxcl12, Mcp1/Ccl2, Socs3, col1a2 and col3a1, Mmp2, Mmp7, a-SMA. Genes were analyzed using the Quantifast SYBR Green PCR Kit (Qiagen) on an ABI 7500 Fast Real-Time System or a Roche LightCycler480 according to the manufacturer's instructions.

Immunohistochemistry

Liver tissue was harvested and fixed overnight in 10% neutral buffered formalin or methacarn solution followed by paraffin embedding. Tissue sections were deparaffinized with xylene and rehydrated using alcohol (100, 75, and 65%). They were then subjected to Ag retrieval by pretreating in a microwave oven with TRIS EDTA (pH 9) for CD3 and Ki67 Ag detection. Ag retrieval for a-SMA, collagen 1, and 3 was performed by preheating sections in a microwave oven with citric acid. The following primary Abs and conditions were used: CD3 (rabbit polyclonal; Abcam), Ki67 (rabbit polyclonal; Dako, discontinued), collagen 1 (131008; 1:100 dilution; formalin-fixed; Ag retrieval; SouthernBiotech), collagen 3 (131001; 1:100 dilution; formalin-fixed; Ag retrieval; SouthernBiotech), α-smooth muscle actin (α-SMA; clone1A4; 1:4000 dilution; formalin-fixed; Ag retrieval; Sigma-Aldrich). Endogenous peroxidase activity was inhibited with 3% hydrogen peroxide, and protein block solution (Dako). To minimize nonspecific binding, normal goat serum was added. Appropriate biotinylated secondary Abs were used. Immunostaining was developed using 3,3′-diaminobenzidine (Dako), and counterstaining with Harris's hematoxylin. Positive cells per area were measured from 20 random fields at ×20 magnification. Sections were photographed using a Nikon Eclipse E600 microscope and NIS-Elements D3.1 Software. H&E staining was performed according to standard protocols. Morphometric pixel analysis to quantify histological staining was performed. For necrosis quantification, H&E-stained sections were scanned to create a single image with Dotslide VS-ASW software (Olympus) using a motorized stage and an Olympus BX51 microscope, acquiring images using an Olympus PlanApo 2× lens and Olympus XC10 camera. Images were analyzed using the Trainable WEKA Segmentation plugin in FIJI. A separate classifier identifying necrotic and viable tissue was determined and applied to all tissue in each image.

Human monocyte–derived macrophages

Human monocyte–derived macrophages (hMDMs) were differentiated from cryopreserved CD14 monocytes essentially as described previously (26). Briefly, cryopreserved stocks were thawed rapidly and diluted in IMEM supplemented with 10% FBS (v/v), 2 mM glutamine, penicillin/streptomycin (500 U/ml, 500 μg/ml), and 100 ng/ml human recombinant CSF1 (Miltenyi) at 2×10^6 cells per ml in Ultra-Low attachment flasks (Corning). Cells were differentiated toward macrophages for 7 d with a 10% media change every second day containing 1 μg CSF1. After 7 d, hMDMs were harvested, counted, and plated on CellCarrier plates for in vitro phagocytosis assays using the Operetta instrument for live imaging (see above).

Zebrafish strain and maintenance

Adult zebrafish (*Danio rerio*) strain TgBAC(csf1ra:GAL4-VP16;UAS:mCherry) (27) were maintained at 28°C and crossed as previously described (28). Embryos were maintained at 28°C and staged according to standard protocols (28).

Zebrafish larval tail fin regeneration assays

Sterile tail fin amputation was performed as previously described (29). Briefly, zebrafish embryos at 2 d postfertilization were anesthetized in 0.3% Danieau's solution containing 0.1 mg/ml tricaine (ethyl 3-aminobenzoate; Sigma-Aldrich) and tail fins were cut off from the end of the notochord using a scalpel. Regeneration was monitored at 24, 48, and 72 h after wounding. Photographs of the regenerating fins were taken at 40× or 50× using a Leica M205 stereomicroscope.

Treatment with small molecules

Next, 5,15-diphenyl-21H,23H-porphine, 5,15-diphenylporphyrin, 5,15-diphenyl-porphine was dissolved in DMSO (stock 10 mM) and diluted to a concentration of 400 μM and 2 mM in 0.3% Danieau's solution. Larvae were treated with compounds at their final concentration immediately after amputation, and media were changed daily with fresh 0.3% Danieau's solution containing the compound.

Statistics

All data are expressed as mean ± SD. The number of replicates is indicated in each figure and each replicate represents a biological rather than an experimental replicate. Data are analyzed and graphs are generated with GraphPad Prism version 5 or 6 (GraphPad Software). Statistic tests have been chosen depending on the biological question behind the experiment. Briefly, we used one- or two-way ANOVA followed by an appropriate posthoc test. The test used is stated in each figure legend. A p value < 0.05 is considered statistically significant.

points (red line) or treated with the vehicle (black line). Blue dots: nonfed BMDMs. Gene expression has been calculated using the ΔΔCT method relative to housekeeping gene Gapdh. (**H**) Socs3 mRNA dosage on RNA from $Gpnmb^+$ and $Gpnmb^-$ BMDMs fed with apoT and treated at the indicated time points. Gene expression has been calculated using the ΔΔCT method relative to housekeeping gene Gapdh. (E–H) The graph reports the ratio between the ΔΔCT of each time point with the ΔΔCT of one of the control (untreated or WT) BMDMs at the same time point.

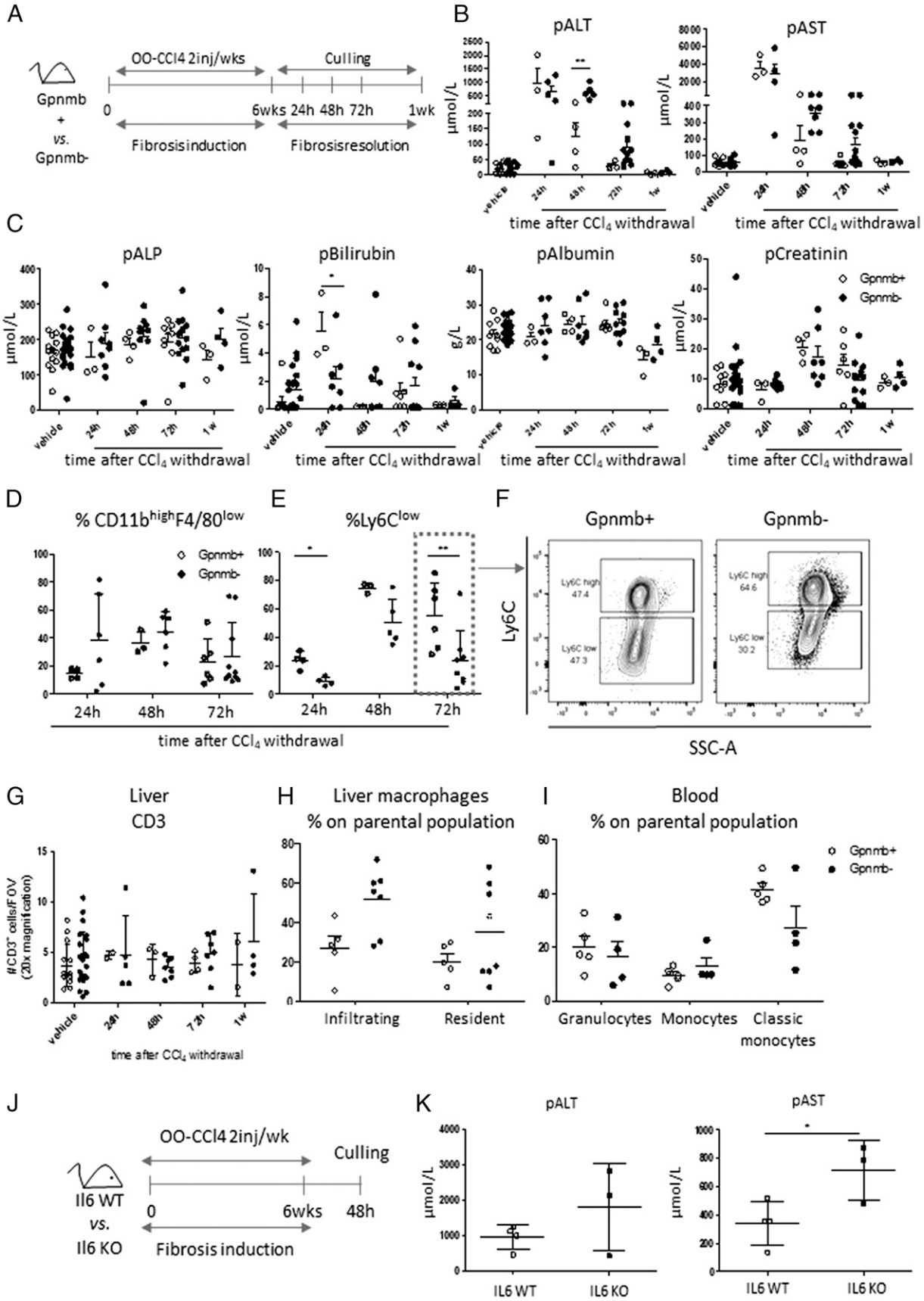

FIGURE 5. Digestion of the phagocytic cargo limits tissue damage and controls macrophage phenotype in a model of chronic sterile liver injury. (**A**) Experimental design. Gpnmb$^+$ (empty dots) and Gpnmb$^-$ (black dots) mice have been treated with CCl_4 twice a week for 6 wk. CCl_4 administration was then discontinued and mice have been culled at 24, 48, 72 h, and 1 wk. (**B**) pALT, pAST dosages at the indicated culling time point in Gpnmb$^+$ (empty dots) and Gpnmb$^-$ (black dots) mice. (**C**) pALP, pBilirubin, pAlbumin, pCreatinine at the indicated culling time point in Gpnmb$^+$ (empty dots) and Gpnmb$^-$ (black dots) mice. Further characterization of the model is reported in Fig. 6 and Supplemental Fig. 3. (**D**) Analysis of *(Figure legend continues)*

We have performed a power calculation for the number of mice to use in the studies on the chronic CCl_4 model based on a pilot study on Gpnmb$^+$ and Gpnmb$^-$ mice on the ALT measure (indicating liver damage) at 48 h after the withdrawal of CCl_4. We have assumed an mu1 of 150 for Gpnmb$^+$ and an mu2 of 600 for Gpnmb$^-$, with a σ of 150. We have set the desired power at 0.80 assuming a statistical significance at the threshold of 0.05. The power calculation returned $n = 3$. This is the minimum number of mice used in each experiment.

For the in vivo phagocytosis there were no preliminary data available. We have treated from a minimum of three to a maximum of seven mice per group. The parameter analyzed for the power calculation is the % of phagocytic infiltrating inflammatory macrophages. If we assume an mu1 (Gpnmb$^+$) of 80 and an mu2 (Gpnmb$^-$) of 20 as derived from our experiment, and a σ of 15, the power calculation for a statistical significance set at 0.05 returns a power of 0.80 with $n = 3$.

We have used six mice per group in the adoptive transfer experiment. Also in this case no preliminary data were available. If we assume an mu1 of 2 for Gpnmb$^+$ and an mu2 of 5 for Gpnmb$^-$, as suggested by our experiment, with a σ of 1.7 and a statistical significance at the threshold of 0.05, the power calculation for a statistical significance set at 0.05 returns a power of 0.80 if $n = 6$ as in our experiment.

For all experiments a two-sided test was considered. All data were tested for normal distribution and equal variance before performing any statistical analysis using Prism v5 or v6. Power calculation has been made using the free online tool available at http://www.stat.ubc.ca.

Results

IL-6 treatment rescues the phenotype of macrophages deficient for phagocytic cargo digestion in vitro and in vivo

To investigate pathways regulating the late stages of efferocytosis, we tested BMDMs from Gpnmb$^+$ and Gpnmb$^-$ mice, which are deficient for the last step of phagocytosis. We analyzed the RNA from Gpnmb$^+$ and Gpnmb$^-$ BMDMs fed with apoTs (apoT) on a low-density qPCR array for inflammatory cytokines and chemokines. One of the most downregulated genes in Gpnmb$^-$ BMDMs is Il-6 (Fig. 1A, 1B, Supplemental Fig. 1A). Gpnmb$^-$ BMDMs are able to initiate efferocytosis but internalization of apoT rapidly tails off (Fig. 1C and gating strategy Supplemental Fig. 1B). Il-6 mRNA is increased at 30 and 60 min after addition of apoT to WT BMDMs (Fig. 1D) and IL-6 protein levels are constant for up to 120 min (Fig. 1E, Supplemental Fig. 1C). This suggests that IL-6 is secreted in a cargo digestion-dependent manner. We hypothesized a role for IL-6 in sustaining efficient efferocytosis in macrophages. To this end, we tested, by flow cytometry, the ability of Gpnmb$^+$ and Gpnmb$^-$ BMDMs to phagocytose apoT in the presence or the absence of increasing concentrations of rmIL-6. rmIL-6 increases the percentage of Gpnmb$^-$ phagocytic BMDMs at any concentration tested (2 h duration of efferocytosis, Fig. 1F). To confirm the role of IL-6 in vivo, we induced acute liver damage by a single injection of CCl_4 in Gpnmb$^+$ and Gpnmb$^-$ mice and we treated them with rmIL-6 or vehicle 6 h prior to culling (Fig. 1G). We digested the livers and analyzed the percentage of infiltrating macrophages by flow cytometry (CD45$^+$Lin$^-$ CD11b^{high}F4/80^{low}). In this gate, we analyzed the percentage of phagocytic (PKH26PCL$^+$), inflammatory (Ly6C^{high}), or restorative (Ly6C^{low}) macrophages. Whereas rmIL-6 treatment did not affect the overall percentage of infiltrating macrophages (Fig. 1H and gating strategy in Supplemental Fig. 1E), it normalized to a WT pattern the phenotype of Gpnmb$^-$–infiltrating inflammatory macrophages in vivo. It had less effect on restorative macrophages (Ly6C^{low}), which infiltrate as inflammatory macrophages before undergoing a phenotypic switch (14) (Fig. 1I and representative plots Fig. 1J).

pSTAT3 is an upstream mediator of IL-6 in efferocytosis

We then analyzed possible pathways upstream of IL-6. Using two inhibitors of NF-κB, we demonstrated that there is no role for this transcription factor in IL-6 regulation of efferocytosis (Supplemental Fig. 1D). IL-6 is one of the cytokine pathways known to induce hepatocyte proliferation in models of hepatocellular carcinoma (HCC) via activation of pSTAT3. In these studies, IL-6 is identified as a single factor coregulating key aspects of macrophage-mediated tissue remodelling and phenotype with epithelial regeneration (30, 31). We tested the hypothesis that this pathway sustains macrophage efferocytosis in a cell-autonomous manner in BMDMs. pSTAT3 blockade resulted in impaired phagocytosis in BMDMs 2 h after the start of phagocytosis (Fig. 2A, 2B) as assessed by flow cytometry. We confirmed the results using live imaging: blocking pSTAT3 impairs phagocytosis of zymosan A–coated, pH sensitive (pHrodo) beads in WT BMDMs and in hMDMs alike (Fig. 2C, 2D), showing the conserved nature of this pathway. In WT BMDMs the impairment is evident as soon as 30–35 min after the start of phagocytosis, and is more complete than blockade of the acidification of the phagosome with bafilomycin (Fig. 2C and Supplemental Videos 1, 2). The pHrodo beads emit fluorescence when in acidic compartments and empty vacuoles are observed in the cytoplasm of BMDMs in the presence of the pSTAT3-blocking peptide (Supplemental Video 3). A similar but less dramatic effect is observed if pSTAT3 is blocked in BMDMs prior to the induction of phagocytosis, indicating that the prophagocytic activity relies mainly on de novo phosphorylated STAT3 (Supplemental Fig. 2A). The blockade of pSTAT3 decreases phagocytosis of infiltrating inflammatory macrophages (Ly6C^{high}) in vivo in a model of acute liver damage induced by CCl_4 injection in which a phagocytic cell tracker is injected (PKH26PCL, for phagocytic cell labeling) (Fig. 2E). The percentage of infiltrating inflammatory macrophages positive for PKH26PCL (i.e., performing phagocytosis) is lower in livers from Gpnmb$^+$ mice treated with the pSTAT3-blocking peptide as compared

the percentage of infiltrating macrophages (CD45$^+$Ly6G$^-$CD11b^{high} F4/80^{low}) in the liver digest of Gpnmb$^+$ (empty dots) and Gpnmb$^-$ (black dots) mice at the indicated time points after the discontinuation of the CCl_4 injection. (**E**) Analysis of the percentage of restorative macrophages (Ly6C^{low}), gated on infiltrating macrophages, in the liver digest of Gpnmb$^+$ (empty dots) and Gpnmb$^-$ (black dots) mice at the indicated time points after the discontinuation of the CCl_4 injection. (**F**) Representative contour plot of the Ly6C expression in infiltrating macrophages in the liver digest of Gpnmb$^+$ and Gpnmb$^-$ mice at 72 h after the discontinuation of the CCl_4 injection (red dotted box in Fig. 4E). (**G**) CD3 immunostaining on sections of liver of Gpnmb$^+$ (empty dots) and Gpnmb$^-$ mice (black dots) treated with CCl4 for 6 wk at distinct time point of recovery and of the same mice treated with olive oil only (vehicle). The number of CD3$^+$ T cells is quantified counting CD3$^+$ nuclei per field of view (FOV) using an original magnification ×20. In total, 20–30 fields per mouse are counted and averaged. Each dot represents the average of one mouse. (**H**) Analysis of the percentage of infiltrating (CD45$^+$Ly6G$^-$CD11b^{high} F4/80^{low}) and resident (CD45$^+$Ly6G$^-$CD11b^{low} F4/80^{high}) macrophages in the liver digest of Gpnmb$^+$ (empty dots) and Gpnmb$^-$ (black dots) mice treated with olive oil only (basal level). (**I**) Analysis of the percentage of granulocytes (CD45$^+$Ly6G$^+$CD11b$^+$), monocytes (CD45$^+$Ly6G$^-$CD11b$^+$CD115$^+$), and classic monocytes (CD45$^+$Ly6G$^-$CD11b$^+$CD115+Ly6C^{high}) in the circulation of Gpnmb$^+$ (empty dots) and Gpnmb$^-$ (black dots) mice treated with olive oil (vehicle) only. (**J**) Experimental design. WT and IL-6 KO mice have been treated with CCl_4 twice a week for 6 wk. CCl_4 administration was then discontinued and mice have been culled at 48 h. (**K**) pALT and pAST dosages at 48 h in IL-6 WT and IL-6 KO mice. (A–E, G–I, and J) Each dot represents a mouse. Average ± SD is shown. Data have been analyzed with two-way ANOVA or Student *t* test for unpaired data when appropriate. Two-way ANOVA is followed by a Bonferroni posthoc test to compare all pairs of columns. Data have been checked for equal variance before further analysis. $*p < 0.05$, $**p < 0.01$.

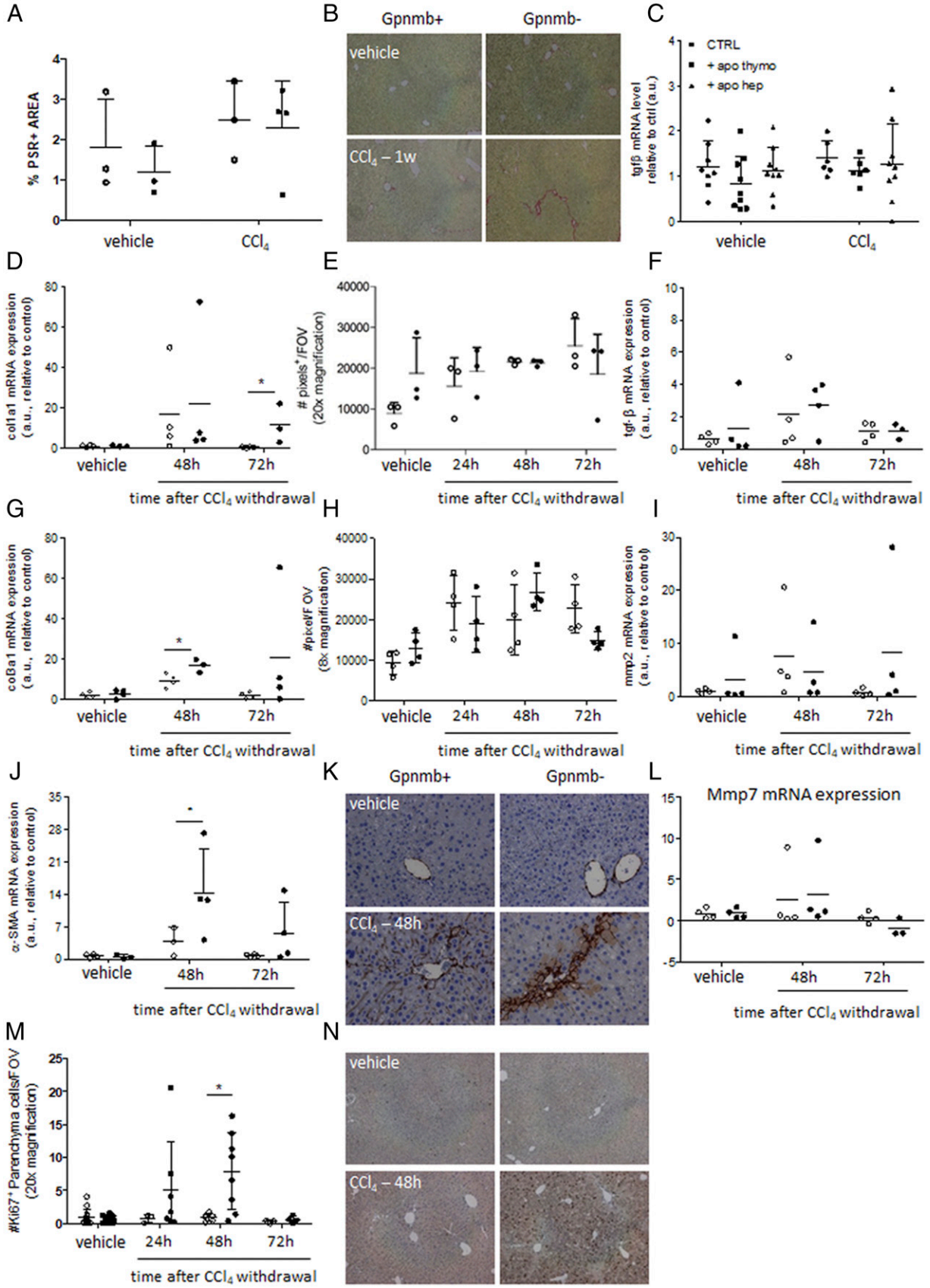

FIGURE 6. Digestion of the phagocytic cargo increases hepatocyte proliferation and not fibrosis in a model of chronic sterile liver injury. (**A**) Fibrosis in the regenerating liver is evaluated at 1 wk after the suspension of the CCl_4 using Sirius-Red staining. Fibrotic septi are distinguished via image analysis and quantified. Original magnification ×20. A minimum of 20 fields per mouse are quantified and averaged. Each dot represents a mouse. (**B**) Representative pictures of the liver of $Gpnmb^+$ and $Gpnmb^-$ mice left untreated or at 1 wk of recovery after CCl_4 discontinuation. (**C**) $Gpnmb^+$ and $Gpnmb^-$ BMDMs are fed with apoTs or hepatocytes (1:5 ratio, BMDMs/apoptotic cells) o.n. Tgf-β mRNA expression is evaluated by qPCR. Each *(Figure legend continues)*

with Gpnmb$^+$ mice treated with an irrelevant peptide, and similar to livers from Gpnmb$^-$ mice (Fig. 2F and representative plot in Fig. 2G). A similar trend is observed in infiltrating restorative macrophages (Fig. 2F). No effect of pSTAT3 inhibition is observed on the overall percentage of resident macrophages (CD45$^+$Ly6G$^-$CD11b^{low}F4/80^{high}), and infiltrating macrophages in Gpnmb$^-$ mice (Fig. 2H, Supplemental Fig. 2B, respectively, and gating strategy in Supplemental Fig. 1E).

STAT3 phosphorylation is required for the maintenance of efficient efferocytosis

To confirm that IL-6 is downstream of pSTAT3, we treated BMDMs with the blocking peptide for pSTAT3, and rescued their phagocytosis using rmIL-6. Live imaging results show that rmIL-6 is able to rescue the BMDM phenotype at 2 h of phagocytosis (Fig. 3A, 3B). The result is confirmed by flow cytometry (Fig. 3C). Two hours after the start of efferocytosis *Il-6* mRNA is reduced in the presence of the pSTAT3 blocking peptide (Fig. 3D); consistently, IL-6 protein shows a reduced trend in the supernatant of phagocytosing BMDMs when pSTAT3 is blocked (Fig. 3E). Therefore, pSTAT3 and IL-6 appear to be in the same pathway, effective in sustaining phagocytosis, with IL-6 controlled at the transcriptional level by pSTAT3 when macrophages are exposed to apoptotic cells for more than 60 min. We then explored the dynamics of pSTAT3 activation upon phagocytosis using flow cytometry, to interrogate the phagocytic fraction of BMDMs (CD11b$^+$CMTMR$^+$). pSTAT3 is activated as early as 7 min after the start of phagocytosis and its activation is sustained at any time point analyzed (Fig. 3F, Supplemental Fig. 2D). Gpnmb$^-$ BMDMs can internalize the cargo but they cannot digest it. Consistent with a role for the pSTAT3–IL-6 axis in sustaining efferocytosis at the cargo digestion stage, pSTAT3 can be activated in Gpnmb$^-$ BMDMs but its activation fails to be sustained at later time points (Fig. 3G, Supplemental Fig. 2E) and pSTAT3 intracellular localization is disrupted in Gpnmb$^-$ BMDMs (Supplemental Fig. 2G). However, analysis of pSTAT3 activation during phagocytosis following rmIL-6 treatment showed no significant difference (data not shown).

pSTAT3 drives IL-10 secretion early after the start of phagocytosis

Later time points of phagocytosis are associated with a cargo digestion-dependent activation of pSTAT3. However, the consequence of the early phosphorylation of STAT3 is thus far unexplored. A target molecule of pSTAT3 is IL-10, and links between IL-10 and phagocytosis have been previously reported (32, 33). We hypothesized that IL-10 could be downstream of pSTAT3 early activation and have a prophagocytic role. To this end, we treated Gpnmb$^+$ and Gpnmb$^-$ BMDMs with rmIL-10 and measured their phagocytic ability. Gpnmb$^+$ BMDMs showed increased phagocytosis at 15 min and Gpnmb$^-$ BMDMs demonstrated a similar trend (Fig. 4A, 4B, Supplemental Fig. 2F). IL-10 protein increased at 15 min in the supernatants of fed BMDMs (Fig. 4C), pointing to a possible early nontranscriptional regulation of IL-10. To confirm a role for pSTAT3 in the regulation of IL-10 secretion early after the start of efferocytosis, we blocked pSTAT3 and measured IL-10 protein in the supernatants of fed WT BMDMs. IL-10 protein dramatically decreases at 15 and 30 min (Fig. 4D). *Il-10* transcription is not induced in BMDMs performing efferocytosis until 30–60 min (Fig. 4E), thereby suggesting a nontranscriptional control of IL-10 secretion by pSTAT3. Consistently, the levels of *Il-10* mRNA are substantially stable when we treat BMDMs with the blocking peptide for pSTAT3 during efferocytosis (Fig. 4F). Thus, pSTAT3 appears to regulate IL-10 release at early stages of efferocytosis in a transcriptionally independent manner. Consistent with a role of IL-10 at early stages of phagocytosis, we did not observe any difference in IL-10 levels in the supernatants of Gpnmb$^+$ and Gpnmb$^-$ macrophages after overnight efferocytosis (Supplemental Fig. 2H). SOCS3 may play a role in macrophage phagocytosis and polarization. Moreover, SOCS3 is known to support IL-6 transcription (34, 35). Consistent with a role of Socs3 in IL-6 production and signaling, we found that Socs3 transcription is controlled by pSTAT3 activation and cargo digestion at 1 h after the start of phagocytosis in BMDMs (Fig. 4G, 4H). To show that the role of pSTAT3 is conserved in tissue repair and remodelling across species, we used the tail fin injury model in *D. rerio* (zebrafish) embryos. *D. rerio* embryos were harvested 48 h postfertilization and we performed the tail injury at the level of the notochord. First, we replicated recent data suggesting that blocking the acidification of intracellular compartments delays tail fin regeneration, a defect similar to that of Gpnmb$^-$ mice (18, 36). To this end, embryos were left to recover from tail fin injury in the presence or absence of bafilomycin to block the acidification of intracellular compartments; length and area of the regenerating fin were recorded at 24, 48, and 72 h postdamage. Treated embryos recapitulated the phenotype of the Gpnmb$^-$ mice with a lower regeneration of the tail fin at 72 h postinjury (data not shown). To test the hypothesis that tail fin remodelling and regeneration is pSTAT3 dependent, we repeated the same experiment monitoring the regrowth of the tail fin in the presence or absence of a small molecule inhibiting pSTAT3, 5,15-diphenyl-21H,23H-porphine, 5,15-diphenylporphyrin, 5,15-diphenyl-porphine (Supplemental Fig. 4F). Reduced tail fin remodelling and regeneration was evident at 24 h after the injury induction. By 48 and 72 h after injury the tail fin remodelling and regeneration was dramatically impaired in terms of both length and area (Supplemental Fig. 4G, 4H). Although we cannot prove that the blockade to tail fin regeneration is macrophage mediated, our data provide a link between pSTAT3 and tissue repair in both zebrafish and mice.

sample is tested in duplicate. Each dot is one sample. Data from two independent experiments are pulled. Mean + SD is reported. (**D**, **F**, **G**, **I**, and **L**) Col1a1, Tgf-b, Col3a1, Mmp2, Mmp7 mRNA expression is evaluated by qPCR on total liver extracts in vehicle-treated mice and at distinct time points after CCl_4 discontinuation. Each mouse is tested in duplicate. Each dot is one mouse. Mean is reported. (**E**–**H**) Quantification of COL1A1 and COL3A1 by immunohistochemistry and image analysis. Original magnification ×20. A minimum 20 fields per mouse are quantified and averaged. Each dot represents a mouse. (**J**) a-SMA mRNA expression is evaluated by qPCR on total liver extracts in vehicle-treated mice and at distinct time points after CCl_4 discontinuation. Each mouse is tested in duplicate. Each dot is one mouse. Mean + SD is reported. (**K**) a-SMA immunohistochemistry. Original magnification ×20. Representative pictures of the livers of Gpnmb$^+$ and Gpnmb$^-$ mice left untreated or at 48 h of recovery after CCl_4 discontinuation. (**M**) Proliferation in the regenerating liver is evaluated at 48 h after the suspension of the CCl4 using immunohistochemistry for Ki67. Parenchymal (hepatocyte) cells are distinguished on the basis of the diameter and quantified. Original magnification 20×. A minimum 20 fields per mouse are quantified and averaged. Each dot represents a mouse. Mean ± SD is reported. (**N**) Representative pictures of the livers of Gpnmb$^+$ and Gpnmb$^-$ mice left untreated or at 48 h of recovery after CCl_4 discontinuation. (A–N) Each dot represents a mouse. Data have been analyzed with two-way ANOVA. Two-way ANOVA is followed by a Bonferroni posthoc test to compare all pairs of columns. Data have been checked for equal variance before further analysis. *$p < 0.05$.

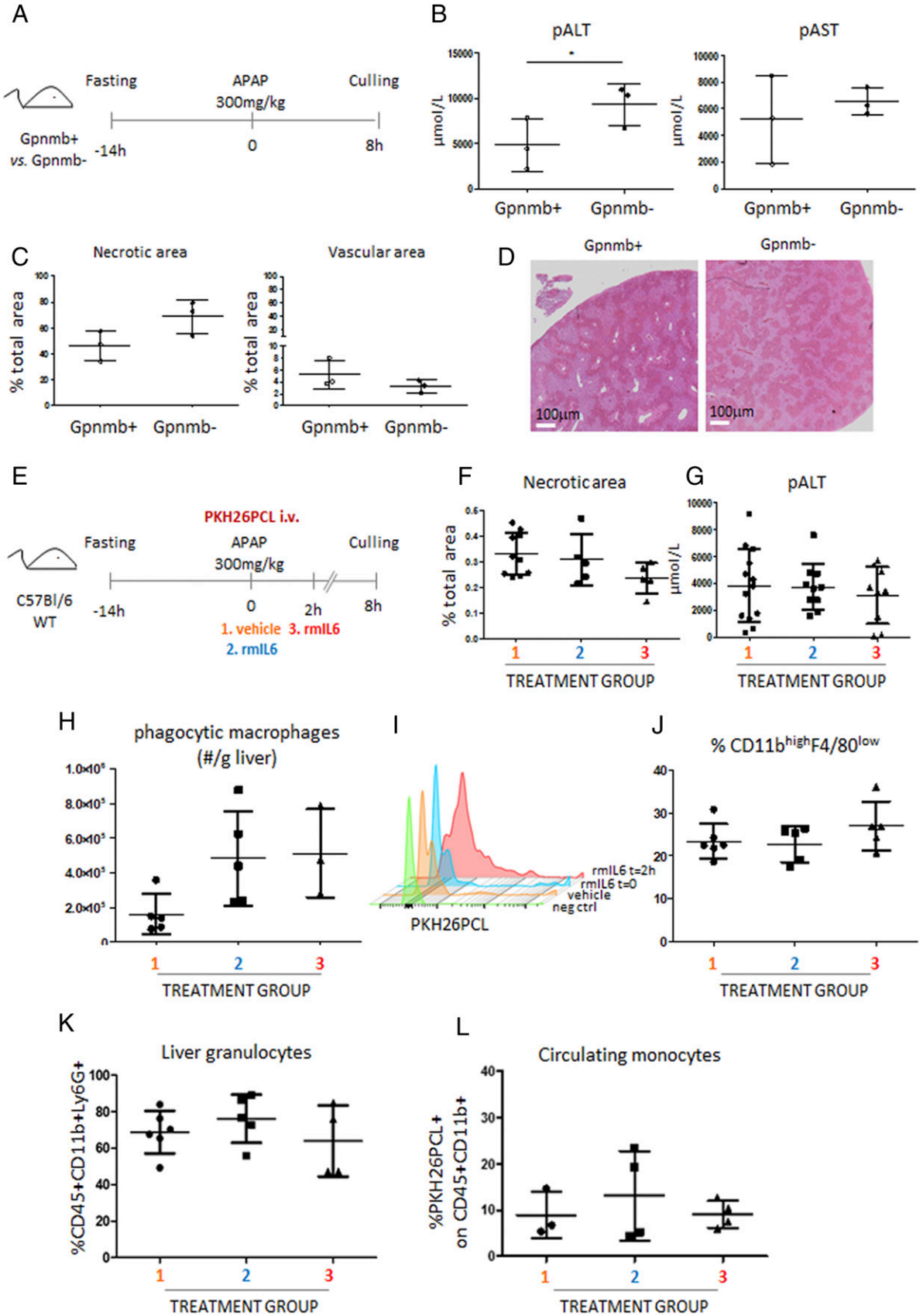

FIGURE 7. Digestion of the phagocytic cargo limits tissue damage in a model of acute liver injury by APAP overdose, and IL-6 treatment improves phagocytosis of infiltrating macrophages. (**A**) Experimental design: Gpnmb$^+$ and Gpnmb$^-$ mice have been starved for 14 h and then dosed with 300 mg/kg of APAP and culled 8 h after liver damage induction. (**B**) pALT and pAST have been measured in Gpnmb$^+$ and Gpnmb$^-$ mice at cull. Each dot represents a distinct mouse. (**C**) Image analysis of H&E-stained sections. Necrotic and vascular area are reported in the left panel, vascular area in the right panel. (**D**) Representative pictures Gpnmb$^+$ (left) and Gpnmb$^-$ (right) livers at 8 h after APAP injection stained with H&E. This is an enlargement of an area of a total-liver picture at original magnification ×4. Full-liver picture is shown in Supplemental Fig. 3E. (**E**) Experimental design: *(Figure legend continues)*

Digestion of the phagocytic cargo limits tissue damage, regulates tissue proliferation, and controls macrophage phenotype in a model of chronic sterile liver injury

Sterile liver injury has proven a useful model to define the interplay of parenchymal cells and inflammation in the mammalian wound-healing response. Therefore, we proceeded to investigate the potential role of cargo digestion during efferocytosis as a regulator of tissue damage and macrophage phenotype in a model of chronic sterile liver injury. We treated Gpnmb$^+$ and Gpnmb$^-$ mice with CCl_4 for 6 wk to induce iterative liver parenchymal sterile necrosis and inflammation with resulting liver fibrosis (Fig. 5A). At the suspension of CCl_4 administration we performed a time-course analysis of circulating pALT and pAST as markers of liver damage, together with pALP, albumin, urea, and creatinine (Fig. 5B, 5C). The liver/body weight ratio was lower in Gpnmb$^-$ mice at 72 h, whereas the two groups of mice show a comparable weight increase during the 6 wk of treatment (Supplemental Fig. 3A, 3B). pALT and pAST are specifically increased in Gpnmb$^-$ mice at 48 h after the suspension of the CCl_4 and the trend is maintained at 72 h. At 1 wk, the levels of ALT and AST are comparable in the two groups of mice. pALP, albumin, urea, and creatinine are unchanged in either genotype at any time point analyzed (Fig. 5B, 5C). We then analyzed the infiltrating macrophages in the damaged liver and the circulating monocytes by flow cytometry (gating strategy in Supplemental Fig. 3C). Failure of phagocytic cargo processing does not affect the general percentage of infiltrating macrophages (live CD45$^+$Ly6G$^-$CD11b^{high}F4/80^{low}) at the basal level and at any time point studied (Fig. 5D, 5H). We then analyzed the percentage of restorative macrophages [which we and others have shown can be identified as Ly6C^{low} (14)]. In Gpnmb$^-$ livers, the percentage of Ly6C^{low} infiltrating macrophages was reduced relative to Gpnmb$^+$ controls at any time point analyzed (Fig. 5E, 5F), suggesting that phagocytosis is a driver of the switch to a Ly6C^{low} restorative macrophage phenotype. Analysis of the expression of liver cytokines and chemokines in the whole liver showed unchanged levels of *Mcp1/Ccl2*, *Cxcl12*, and *Hmgb1* (Supplemental Fig. 3D). Consistent with the lack of difference in the overall infiltration of macrophages, T lymphocyte infiltrate was comparable in the two groups of mice at all time points analyzed and at basal level (Fig. 5G). Circulating granulocytes, monocytes, and, particularly, classic monocytes were similar in the two groups of mice (Fig. 5I). Overall, the impairment in phagocytic cargo processing caused increased liver damage and prevented macrophage phenotype switching during regeneration. If IL-6 has a prophagocytic role relevant for the clearance of damaged cells, then we would expect an increase in damage in the livers of IL-6 KO mice with iterative sterile injury (Fig. 5J). Supporting this model and directly reproducing the phenotype observe in Gpnmb$^-$ mice, IL-6 KO mice showed higher levels of circulating ALT and AST at 48 h after CCl_4 withdrawal, without showing any difference in the level of pALP (Fig. 5K) or in their liver/body weight ratio (Supplemental Fig. 4A).

We then verified the impact of impaired phagocytic cargo processing on liver pathology. At 1 wk of recovery, there is no difference in fibrosis between the two groups of mice (Fig. 6A, 6B). Gpnmb$^-$ BMDMs showed similar level of Tgf-β when compared with Gpnmb$^+$ BMDMs after overnight phagocytosis (Fig. 6C). Further, the lack of difference in liver fibrosis between the two groups of mice was confirmed by collagen 1, Tgf-β, Mmp-2, and Mmp-7 mRNA analysis (Fig. 6D, 6F, 6I, 6L). Col3a1 mRNA was increased at 48 h (Fig. 6G), but no differences between the two groups of mice were observed in the immunohistochemical analysis (Fig. 6H). However, Gpnmb$^-$ livers show increased α-SMA levels at 48 h of recovery (Fig. 6J, 6K). The similar levels of liver fibrosis in Gpnmb$^-$ mice may result in part from the increased proliferation of parenchymal cells at 48 h of recovery (Fig. 6M, 6N).

Digestion of the phagocytic cargo limits tissue damage in a model of acute liver injury by APAP overdose, and IL-6 treatment improves phagocytosis of infiltrating macrophages

We collected further evidence for a correlation between phagocytosis, IL-6, and damage resolution in a clinically relevant model of sterile acute liver damage by APAP intoxication (Fig. 7A), which is characterized by extensive parenchymal cell death and inflammation (37, 38). Gpnmb$^-$ mice have a higher level of pALT at 8 h postinjury (Fig. 7B); consistently, they showed a more extended necrotic area than their Gpnmb$^+$ counterparts as assessed by image analysis (Fig. 7C, 7D and Supplemental Fig. 3E). We then dosed C57BL/6 WT mice with APAP and treated them with rmIL-6 at the same time as, or 2 h after, the APAP injection. To track phagocytic cells, we injected PKH26PCL into some of the mice, which were culled at 8 h after APAP dosing to quantify the effect of rmIL-6 treatment on the phagocytic ability of infiltrating macrophages (Fig. 7E). We did not observe a significant effect of IL-6 treatment on the necrotic area, the pALT or the liver/body weight ratio (Fig. 7F, 7G, Supplemental Fig. 4B). Importantly, the number of phagocytic macrophages per gram of liver was increased in rmIL-6–injected mice (Fig. 7H, 7I). The treatment was efficacious in increasing macrophage phagocytosis without affecting the percentage of infiltrating macrophages and granulocytes in the damaged liver (Fig. 7J, 7K). The local effect of the systemic treatment with rmIL-6 is confirmed by a lack of effect on the phagocytic ability of circulating monocytes (Fig. 7L).

Phagocytosis drives the conversion of inflammatory into restorative macrophages

To test the hypothesis that the prophagocytic positive feedback loop triggered by the STAT3–IL-6 axis drives the conversion of macrophage phenotype, and thereby provides a link between tissue

Gpnmb$^+$ and Gpnmb$^-$ mice have been starved for 14 h and then dosed with 300 mg/kg of APAP and culled 8 h after liver damage induction. Saline (vehicle, treatment group 1) or rmIL-6 have been injected i.p. at the same time as APAP injection (treatment group 2) or 2 h later (treatment group 3). (**F**) Image analysis of H&E-stained sections. Each dot is a distinct mouse. Mean ± SD of the necrotic area is reported. (**G**) Average ± SD of the pALT is reported. Each dot represents a distinct mouse. (**H**) Average ± SD of the number (#) per gram of liver of infiltrating phagocytic macrophages (CD45$^+$Lin$^-$ CD11b^{high}, F4/80$^{low/int}$, PKH26PCL$^+$) is reported. Each dot is a distinct mouse. (**I**) Representative histogram plots for PKH26PCL in the gate of infiltrating macrophages in a PKH26PCL uninjected mouse (neg ctrl) and in the three groups of mice analyzed. (**J**) Average ± SD of the percentage of infiltrating macrophages (CD11b^{high}, F4/80^{low}) in the gate of CD45+Lin$^-$ cells is reported. Each dot is a distinct mouse. (**K**) Granulocyte percentage on the parental population is calculated in liver digest of mice dosed with APAP 300 mg/kg and injected with saline (treatment group 1), rmIL-6 at the time of APAP injection (treatment group 2), and 2 h after the APAP injection (treatment group 3). (**L**) Percentage of phagocytic (PKH26PCL$^+$) bona fide circulating monocytes (CD45$^+$CD11b$^+$Ly6G$^-$) at the time of culling in the blood of mice dosed with APAP 300 mg/kg and injected with saline (treatment group 1), rmIL-6 at the time of APAP injection (treatment group 2), and 2 h after the APAP injection (treatment group 3). (B, C, F–H, and J–L) Data have been analyzed with Student *t* test or two-way ANOVA for unpaired data when appropriate, followed by a Bonferroni posthoc test to compare all pairs of columns. Data have been checked for equal variance before further analysis. $*p < 0.05$.

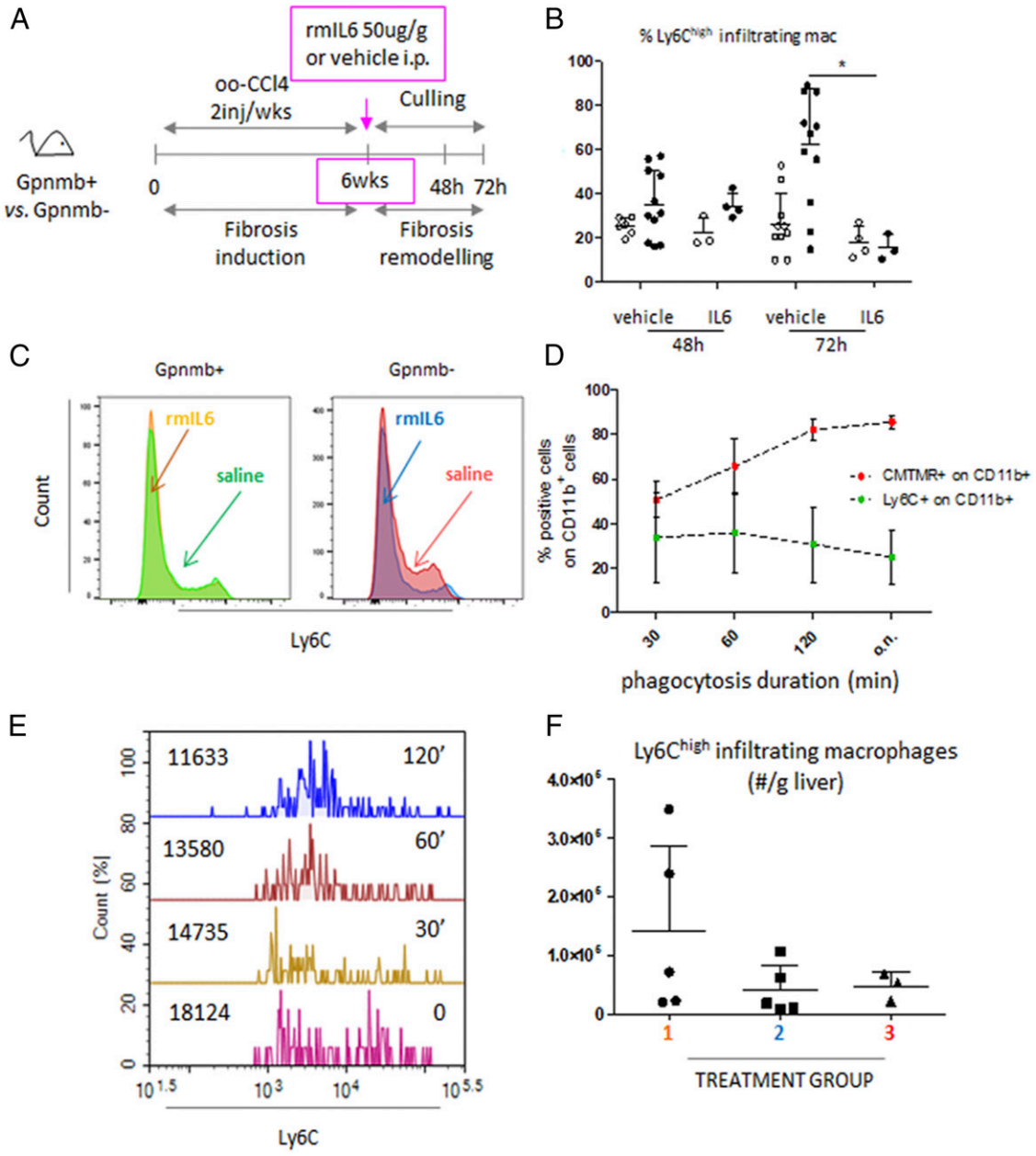

FIGURE 8. Phagocytosis drives the conversion of inflammatory to restorative macrophages. (**A**) Experimental design: chronic CCl_4 administration followed by the injection of rmIL-6 or vehicle (saline, sham treated mice) i.p. at the suspension of CCl_4. Mice have been culled 48 and 72 h later. Livers have been harvested, digested, and labeled for flow cytometry. (**B**) Flow cytometry analysis of liver digest. Infiltrating macrophages have been identified as described in Supplemental Fig. 3 and inflammatory macrophages are identified as percentage of $Ly6C^{high}$ events in the gate of infiltrating macrophages. White dots: $Gpnmb^{+}$ mice. Black dots: $Gpnmb^{-}$ mice. Each dot is a distinct mouse. Average ± SD are reported. Data have been analyzed with two-way ANOVA for unpaired data followed by a Bonferroni posthoc test to compare all columns with the control column. $*p < 0.05$. (**C**) Representative histogram plots of Ly6C fluorescence in the gate of infiltrating macrophages in the liver digest of $Gpnmb^{+}$ and $Gpnmb^{-}$ mice. (**D**) Green: expression of Ly6C in BMDM subjected to phagocytosis of apoTs at the indicated time point. Red: percentage of phagocytic BMDMs, calculated on the same population analyzed for Ly6C expression. Average ± SD is reported. $n = 3$. (**E**) Representative histogram plot of Ly6C expression at distinct time points after the start of phagocytosis. We report mean fluorescence intensity values on the left and the time point analyzed on the right. (**F**). Number (#) per gram of liver of $Ly6C^{high}$ infiltrating macrophages in APAP-dosed mice untreated (1, orange) or treated with rmIL-6 at the moment of APAP injection (2, light blue) or 2 h later (3, red). Each dot is a distinct mouse. Average + SD are reported.

damage and tissue repair, we administered rmIL-6 to $Gpnmb^{+}$ and $Gpnmb^{-}$ mice after induction of chronic liver injury by CCl_4. Mice were culled at 48 and 72 h after CCl_4 withdrawal (Fig. 8A). rmIL-6 restored the ability of $Gpnmb^{-}$ mice to convert the inflammatory $Ly6C^{high}$ macrophages into restorative $Ly6C^{low}$ macrophages within 72 h of administration (Fig. 8B, 8C). Consistent with a reprogramming action of phagocytosis, WT BMDMs fed with CMTMR-labeled apoTs showed a sharp decrease of the percentage of $Ly6C^{high}$ events; i.e., bona fide inflammatory BMDMs were reduced just as the percentage of phagocytic BMDMs increased in the population (Fig. 8D, 8E). Independent evidence was sought by treating APAP-dosed mice with rmIL-6 at distinct time points (Fig. 7E). The number of $Ly6C^{high}$ infiltrating macrophages (i.e., infiltrating inflammatory macrophages) was lower in mice treated with rmIL-6 (Fig. 8F), which also showed a higher number of phagocytic macrophages infiltrating the liver

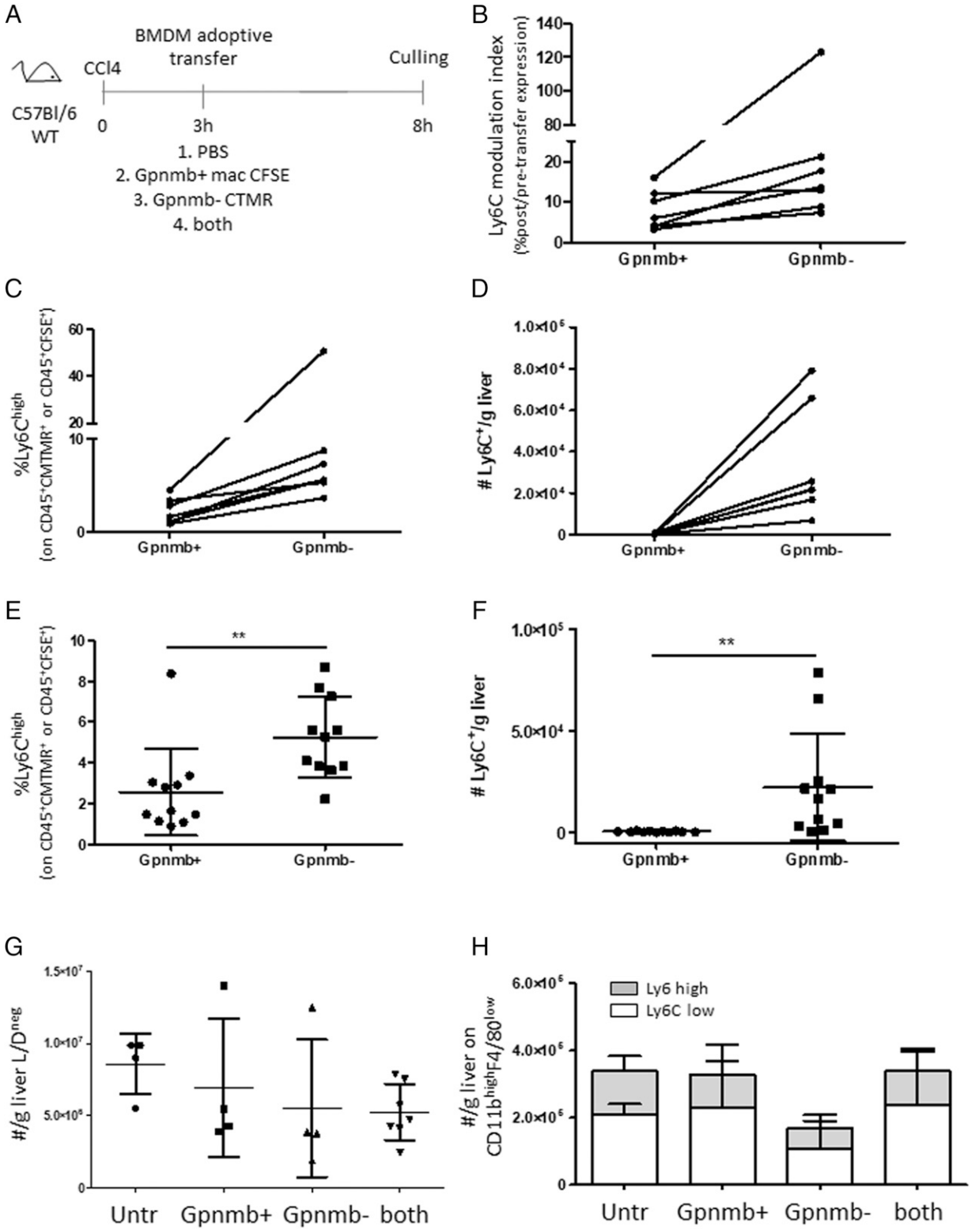

FIGURE 9. Phagocytosis drives the conversion of inflammatory to restorative macrophages in a cell-autonomous manner. (**A**) Experimental design: single CCl_4 injection is followed 3 h later by adoptive transfer of BMDMs. Group 1: PBS; group 2: Gpnmb$^+$ BMDMs labeled with CFSE; group 3: Gpnmb$^-$ BMDMs labeled with CMTR; group 4: both populations in equal number. The experiment has been repeated with Gpnmb$^+$ CMTMR BMDMs and Gpnmb$^-$ CFSE BMDMs. Then 8 h after CCl_4 injection mice have been culled, the livers harvested, digested, and labeled for flow cytometry analysis. (**B**) Ly6C modulation index = Ly6C expression in the Gpnmb$^+$ or Gpnmb$^-$ gate/Ly6C expression pretransplant. Each couple of data represent the level of Ly6C of BMDMs transferred in the same mouse (group 4). (**C**) Percentage of Ly6C^{high} in the transplanted population, without considering the levels of Ly6C expression pretransplant. Each dot on the left is the percentage of Gpnmb$^+$ Ly6C^{high} in one transplanted mouse. Each connected dot on the right is the percentage of Gpnmb$^-$ Ly6C^{high} in the same transplanted mouse. (**D**) Same analysis as in (C) carried out using the number of Ly6C^{high} transferred BMDMs. (**E**) Analysis of the percentage of Ly6C^{high} events in the gate of Gpnmb$^+$ or Gpnmb$^-$ adoptively transferred BMDMs, including mice that received only one of the two populations (group 2 + 4 versus group 3 + 4). Mean and SD are reported. Data are analyzed by *t* test for unpaired data after the distribution is checked for equal variance. $^{**}p = 0.01$. (**F**) Same analysis as in (E) carried out using the number of Ly6C^{high} transferred BMDM. (**G**) The mean and SD of the number of live cells per gram liver is reported. Each dot is a mouse. (**H**) Number (#) of Ly6C^{high} and Ly6C^{low} infiltrating (CD11b^{high}-F4/80^{low}) macrophages per gram of liver in mice receiving PBS (uninjected), Gpnmb$^+$ BMDMs only (Gpnmb$^+$), Gpnmb$^-$ BMDMs only (Gpnmb$^-$), or both populations (both).

(Fig. 7H). To demonstrate that phagocytosis triggers a macrophage-phenotypic switch, we induced acute damage by a single injection of CCl_4 in C57BL/6 mice. After 3 h, we adoptively transferred $CFSE^+Gpnmb^+$ and $CMTMR^+Gpnmb^-$ BMDMs separately, or mixed in 1:1 ratio. Then 5 h later mice are culled, the liver digested, and cells analyzed (Fig. 9A, gating strategy in Supplemental Fig. 4C). Macrophage conversion to a restorative phenotype was monitored using the level of Ly6C expression. The percentage of $Ly6C^{high}$ adoptively transferred macrophages was calculated in $Gpnmb^+$ and $Gpnmb^-$ BMDMs before and after transplant. Both genotypes showed a lower posttransfer percentage of $Ly6^{high}$ transferred macrophages as compared with pretransfer (Fig. 9B). However, adoptively transferred $Gpnmb^-$ macrophages showed a consistently higher percentage of $Ly6C^{high}$ cells versus their $Gpnmb^+$ counterparts cotransferred in the same mouse and therefore in an identical microenvironment (Fig. 9B–D). The higher percentage of $Ly6C^{high}$ cells in $Gpnmb^-$ macrophages was also confirmed when the data from the mice receiving only $Gpnmb^+$ or $Gpnmb^-$ BMDMs were included in the analysis (Fig. 9E, 9F). The transfer of $Gpnmb^-$ BMDMs reduced the hepatic recruitment of the endogenous macrophages: host livers showing a lower number of both $Ly6C^{high}$ and $Ly6C^{low}$ infiltrating macrophages and a contraction of the $Ly6C^{low}$ population (Fig. 9H). The difference observed was not due to a difference in the viability of extracted cells (Fig. 9G, Supplemental Fig. 4D, 4E).

Discussion

Our data suggest that the processing of apoptotic cells activates a STAT3–IL-10–IL-6 autocrine-paracrine loop, enabling macrophages to maintain their scavenging ability. Furthermore, a failure of phagocytic cargo processing results in the reduced uptake of debris (predominantly in proinflammatory macrophages), prolonged liver damage, enhanced hepatocyte proliferation, and a reduced expression of IL-10. These data suggest that macrophage ingestion of apoptotic cell and IL-6 production are important for debris clearance and the phenotypic switch to a restorative phenotype. Apoptotic cells are necessary to trigger an IL-4/IL-13–dependent tissue repair response in models of helminth infection (39). In this study, we provide data linking an immediate event in proinflammatory macrophages to the programming of tissue remodelling and regeneration in the context of sterile injury. Phagocytosis of apoptotic bodies (efferocytosis) may require the presence of autophagy-related molecules for the assembly of the phagosome, a process named LC3-associated phagocytosis (40). During LC3-associated phagocytosis some of the autophagy machinery, including LC3, is recruited to pathogen, apoptotic, and necrotic cell-containing phagosomes; as a result, optimal degradation of the phagocytosed cargo is achieved (41, 42). Gpnmb is an interactor of LC3 (18), making $Gpnmb^-$ mice a useful model to study the effect of an incomplete phagocytic process of apoptotic cells on sterile injury and repair models.

In our model, STAT3, IL-10, and IL-6 are in the same pathway and provide mechanistic insight on previous observations that correlated IL-10 and phagocytosis in in vitro models (32, 33, 43, 44). Our work provides a mechanistic explanation to recent data regarding the restorative role of $Gpnmb^+$ macrophages in acute liver (45) and kidney injuries (18), and in DSS-induced colitis (46); and the proresolution role of $Gpnmb^+$ macrophages in a model of peritonitis (47). Growing evidence correlates pSTAT3 activation with tumor cell proliferation, genomic instability, and migration (48–53). In addition, recent studies establish a link between pSTAT3 activation and immunomodulation in tumors, via infiltrating monocytes switching phenotype to tumor-associated macrophages (54–57). Moreover, the IL-10–IL-6–pSTAT3 pathway has been reported as having a role in the inflammatory process in inflamed adipose tissue from obese patients (58). Our data suggest pSTAT3 acts as a driver of inflammatory macrophage phagocytosis and phenotypic conversion. Although the switch to an anti-inflammatory, pro-remodeling phenotype is detrimental in tumor models (11, 59), it is required in physiological tissue repair (1, 9). The completion of a correct phagocytic process leads macrophages to switch their inflammatory phenotype into a restorative one, evidencing that phagocytosis is a major process through which the initial damage phase initiates the repair of the tissue. Our in vitro data and in vivo adoptive transfer show this process happens soon after the induction of damage. The identification of phagocytosis as a key element mediating macrophage phenotype conversion is of therapeutic relevance for a number of diseases. Means to increase restorative-like macrophage phenotype have proved beneficial to block CNS inflammation (60), systemic lupus erythematosus (61), and to contribute to hepatic progenitor cell specification in models of liver disease (16, 62). STAT3-IL-6 is a pro-proliferative signal in HCC development. Tumor-associated macrophages in HCC have a phenotype similar to restorative macrophages (63). Macrophages forced to stay in an inflammatory phenotype downregulate Stat3 and have a higher anti-HCC activity (64). Our data linking a STAT3–IL-10–IL-6 positive feedback loop with phagocytosis enhancement and a macrophage phenotypic switch may also explain recent data showing that IL-6–producing macrophages, polarized with rIL-4, block neuroinflammation in vivo (65). The possible link between STAT3–IL-10–IL-6 and the control of hepatocyte proliferation is worthy of further investigation. Macrophages link tissue necrosis and repair in many diseases; explaining how to program their regenerative response via the control of their ability to scavenge dead cells will be important for future therapeutic targeting in multiple clinical settings, which may include acute liver injury and chronic liver fibrosis.

Acknowledgments

We thank Dr. William Ramsay and Dr. Shonna Johnston at the Flow Cytometry Facility of the Queen's Medical Research Institute of the University of Edinburgh for the technical assistance during the first part of the project. We thank Dr. Fiona Rossi and Dr. Clare Cryer at the Flow Cytometry Facility of the Medical Research Council Centre for Regenerative Medicine of the University of Edinburgh for technical assistance during the second part of the project. We thank the Shared University Research Facilities at the University of Edinburgh for assistance with histology and qPCR. We thank Dr. Bertrand Vernay at the Imaging Facility of the Medical Research Council Centre for Regenerative Medicine of the University of Edinburgh for support with the confocal imaging. We thank the technicians in the animal units of Little France and of the Tissue Culture Unit of the Medical Research Council Centre for Regenerative Medicine for continuous help and support throughout the project. In particular, we thank Laraine Wells, William Mungall, Lynn, and Theresa O'Connor.

Disclosures

The authors have no financial conflicts of interest.

References

1. Savill, J., I. Dransfield, C. Gregory, and C. Haslett. 2002. A blast from the past: clearance of apoptotic cells regulates immune responses. *Nat. Rev. Immunol.* 2: 965–975.
2. Elliott, M. R., and K. S. Ravichandran. 2010. Clearance of apoptotic cells: implications in health and disease. *J. Cell Biol.* 189: 1059–1070.
3. Baruah, P., I. E. Dumitriu, G. Peri, V. Russo, A. Mantovani, A. A. Manfredi, and P. Rovere-Querini. 2006. The tissue pentraxin PTX3 limits C1q-mediated complement activation and phagocytosis of apoptotic cells by dendritic cells. *J. Leukoc. Biol.* 80: 87–95.
4. Bondanza, A., V. S. Zimmermann, P. Rovere-Querini, J. Turnay, I. E. Dumitriu, C. M. Stach, R. E. Voll, U. S. Gaipl, W. Bertling, E. Pöschl, et al. 2004. Inhibition of phosphatidylserine recognition heightens the immunogenicity of irradiated lymphoma cells in vivo. *J. Exp. Med.* 200: 1157–1165.

5. Rovere-Querini, P., and I. E. Dumitriu. 2003. Corpse disposal after apoptosis. *Apoptosis* 8: 469–479.
6. Yamaguchi, H., T. Fujimoto, S. Nakamura, K. Ohmura, T. Mimori, F. Matsuda, and S. Nagata. 2010. Aberrant splicing of the milk fat globule-EGF factor 8 (MFG-E8) gene in human systemic lupus erythematosus. *Eur. J. Immunol.* 40: 1778–1785.
7. Green, D. R., T. H. Oguin, and J. Martinez. 2016. The clearance of dying cells: table for two. *Cell Death Differ.* 23: 915–926.
8. Poon, I. K., C. D. Lucas, A. G. Rossi, and K. S. Ravichandran. 2014. Apoptotic cell clearance: basic biology and therapeutic potential. *Nat. Rev. Immunol.* 14: 166–180.
9. Serhan, C. N., and J. Savill. 2005. Resolution of inflammation: the beginning programs the end. *Nat. Immunol.* 6: 1191–1197.
10. Yin, C., Y. Kim, D. Argintaru, and B. Heit. 2016. Rab17 mediates differential antigen sorting following efferocytosis and phagocytosis. *Cell Death Dis.* 7: e2529.
11. Mosser, D. M., and J. P. Edwards. 2008. Exploring the full spectrum of macrophage activation. *Nat. Rev. Immunol.* 8: 958–969.
12. Mantovani, A., A. Sica, S. Sozzani, P. Allavena, A. Vecchi, and M. Locati. 2004. The chemokine system in diverse forms of macrophage activation and polarization. *Trends Immunol.* 25: 677–686.
13. Lucas, M., L. M. Stuart, A. Zhang, K. Hodivala-Dilke, M. Febbraio, R. Silverstein, J. Savill, and A. Lacy-Hulbert. 2006. Requirements for apoptotic cell contact in regulation of macrophage responses. *J. Immunol.* 177: 4047–4054.
14. Ramachandran, P., A. Pellicoro, M. A. Vernon, L. Boulter, R. L. Aucott, A. Ali, S. N. Hartland, V. K. Snowdon, A. Cappon, T. T. Gordon-Walker, et al. 2012. Differential Ly-6C expression identifies the recruited macrophage phenotype, which orchestrates the regression of murine liver fibrosis. *Proc. Natl. Acad. Sci. USA* 109: E3186–E3195.
15. Baeck, C., X. Wei, M. Bartneck, V. Fech, F. Heymann, N. Gassler, K. Hittatiya, D. Eulberg, T. Luedde, C. Trautwein, and F. Tacke. 2014. Pharmacological inhibition of the chemokine C-C motif chemokine ligand 2 (monocyte chemoattractant protein 1) accelerates liver fibrosis regression by suppressing Ly-6C(+) macrophage infiltration in mice. *Hepatology* 59: 1060–1072.
16. Boulter, L., O. Govaere, T. G. Bird, S. Radulescu, P. Ramachandran, A. Pellicoro, R. A. Ridgway, S. S. Seo, B. Spee, N. Van Rooijen, et al. 2012. Macrophage-derived Wnt opposes Notch signaling to specify hepatic progenitor cell fate in chronic liver disease. *Nat. Med.* 18: 572–579.
17. Anderson, M. G., R. S. Smith, N. L. Hawes, A. Zabaleta, B. Chang, J. L. Wiggs, and S. W. John. 2002. Mutations in genes encoding melanosomal proteins cause pigmentary glaucoma in DBA/2J mice. *Nat. Genet.* 30: 81–85.
18. Li, B., A. P. Castano, T. E. Hudson, B. T. Nowlin, S. L. Lin, J. V. Bonventre, K. D. Swanson, and J. S. Duffield. 2010. The melanoma-associated transmembrane glycoprotein Gpnmb controls trafficking of cellular debris for degradation and is essential for tissue repair. *FASEB J.* 24: 4767–4781.
19. Assunção-Miranda, I., F. A. Amaral, F. A. Bozza, C. T. Fagundes, L. P. Sousa, D. G. Souza, P. Pacheco, G. Barbosa-Lima, R. N. Gomes, P. T. Bozza, et al. 2010. Contribution of macrophage migration inhibitory factor to the pathogenesis of dengue virus infection. *FASEB J.* 24: 218–228.
20. Bain, C. C., C. A. Hawley, H. Garner, C. L. Scott, A. Schridde, N. J. Steers, M. Mack, A. Joshi, M. Guilliams, A. M. Mowat, et al. 2016. Long-lived self-renewing bone marrow-derived macrophages displace embryo-derived cells to inhabit adult serous cavities. *Nat. Commun.* 7: ncomms11852.
21. Bergmeyer, H. U., P. Scheibe, and A. W. Wahlefeld. 1978. Optimization of methods for aspartate aminotransferase and alanine aminotransferase. *Clin. Chem.* 24: 58–73.
22. Pearlman, F. C., and R. T. Lee. 1974. Detection and measurement of total bilirubin in serum, with use of surfactants as solubilizing agents. *Clin. Chem.* 20: 447–453.
23. Campana, L., F. Santarella, A. Esposito, N. Maugeri, E. Rigamonti, A. Monno, T. Canu, A. Del Maschio, M. E. Bianchi, A. A. Manfredi, and P. Rovere-Querini. 2014. Leukocyte HMGB1 is required for vessel remodeling in regenerating muscles. *J. Immunol.* 192: 5257–5264.
24. Ferenbach, D. A., V. Ramdas, N. Spencer, L. Marson, I. Anegon, J. Hughes, and D. C. Kluth. 2010. Macrophages expressing heme oxygenase-1 improve renal function in ischemia/reperfusion injury. *Mol. Ther.* 18: 1706–1713.
25. Bosurgi, L., S. Brunelli, E. Rigamonti, A. Monno, A. A. Manfredi, and P. Rovere-Querini. 2015. Vessel-associated myogenic precursors control macrophage activation and clearance of apoptotic cells. *Clin. Exp. Immunol.* 179: 62–67.
26. Moore, J. K., A. C. Mackinnon, D. Wojtacha, C. Pope, A. R. Fraser, P. Burgoyne, L. Bailey, C. Pass, A. Atkinson, N. W. Mcgowan, et al. 2015. Phenotypic and functional characterization of macrophages with therapeutic potential generated from human cirrhotic monocytes in a cohort study. *Cytotherapy* 17: 1604–1616.
27. Gray, C., C. A. Loynes, M. K. Whyte, D. C. Crossman, S. A. Renshaw, and T. J. Chico. 2011. Simultaneous intravital imaging of macrophage and neutrophil behaviour during inflammation using a novel transgenic zebrafish. *Thromb. Haemost.* 105: 811–819.
28. Westerfield, M. 2000. *The zebrafish Book: A Guide for the Laboratory Use of D. rerio (zebrafish).* University of Oregon Press, Eugene, OR.
29. Renshaw, S. A., C. A. Loynes, D. M. Trushell, S. Elworthy, P. W. Ingham, and M. K. Whyte. 2006. A transgenic zebrafish model of neutrophilic inflammation. *Blood* 108: 3976–3978.
30. Ezure, T., T. Sakamoto, H. Tsuji, J. G. Lunz, III, N. Murase, J. J. Fung, and A. J. Demetris. 2000. The development and compensation of biliary cirrhosis in interleukin-6-deficient mice. *Am. J. Pathol.* 156: 1627–1639.
31. Michalopoulos, G. K., and M. C. DeFrances. 1997. Liver regeneration. *Science* 276: 60–66.
32. Capsoni, F., F. Minonzio, A. M. Ongari, V. Carbonelli, A. Galli, and C. Zanussi. 1995. IL-10 up-regulates human monocyte phagocytosis in the presence of IL-4 and IFN-gamma. *J. Leukoc. Biol.* 58: 351–358.
33. Petit-Bertron, A. F., C. Fitting, J. M. Cavaillon, and M. Adib-Conquy. 2003. Adherence influences monocyte responsiveness to interleukin-10. *J. Leukoc. Biol.* 73: 145–154.
34. Qin, H., A. T. Holdbrooks, Y. Liu, S. L. Reynolds, L. L. Yanagisawa, and E. N. Benveniste. 2012. SOCS3 deficiency promotes M1 macrophage polarization and inflammation. *J. Immunol.* 189: 3439–3448.
35. Gordon, P., B. Okai, J. I. Hoare, L. P. Erwig, and H. M. Wilson. 2016. SOCS3 is a modulator of human macrophage phagocytosis. *J. Leukoc. Biol.* 100: 771–780.
36. Varga, M., M. Sass, D. Papp, K. Takács-Vellai, J. Kobolak, A. Dinnyés, D. J. Klionsky, and T. Vellai. 2014. Autophagy is required for zebrafish caudal fin regeneration. *Cell Death Differ.* 21: 547–556.
37. Krenkel, O., J. C. Mossanen, and F. Tacke. 2014. Immune mechanisms in acetaminophen-induced acute liver failure. *Hepatobiliary Surg. Nutr.* 3: 331–343.
38. Mossanen, J. C., and F. Tacke. 2015. Acetaminophen-induced acute liver injury in mice. *Lab. Anim.* 49(1 Suppl.): 30–36.
39. Bosurgi, L., Y. G. Cao, M. Cabeza-Cabrerizo, A. Tucci, L. D. Hughes, Y. Kong, J. S. Weinstein, P. Licona-Limon, E. T. Schmid, F. Pelorosso, et al. 2017. Macrophage function in tissue repair and remodeling requires IL-4 or IL-13 with apoptotic cells. *Science* 356: 1072–1076.
40. Preaux, A. M., M. P. D'ortho, M. P. Bralet, Y. Laperche, and P. Mavier. 2002. Apoptosis of human hepatic myofibroblasts promotes activation of matrix metalloproteinase-2. *Hepatology* 36: 615–622.
41. Martinez, J., J. Almendinger, A. Oberst, R. Ness, C. P. Dillon, P. Fitzgerald, M. O. Hengartner, and D. R. Green. 2011. Microtubule-associated protein 1 light chain 3 alpha (LC3)-associated phagocytosis is required for the efficient clearance of dead cells. *Proc. Natl. Acad. Sci. USA* 108: 17396–17401.
42. Martinez, J., R. K. Malireddi, Q. Lu, L. D. Cunha, S. Pelletier, S. Gingras, R. Orchard, J. L. Guan, H. Tan, J. Peng, et al. 2015. Molecular characterization of LC3-associated phagocytosis reveals distinct roles for Rubicon, NOX2 and autophagy proteins. *Nat. Cell Biol.* 17: 893–906.
43. Tassiulas, I., K. H. Park-Min, Y. Hu, L. Kellerman, D. Mevorach, and L. B. Ivashkiv. 2007. Apoptotic cells inhibit LPS-induced cytokine and chemokine production and IFN responses in macrophages. *Hum. Immunol.* 68: 156–164.
44. Kamdar, S. J., J. A. Fuller, and R. Evans. 1997. CSF-1-induced and constitutive Il6 gene expression in mouse macrophages: evidence for PKC-dependent and -independent pathways. *Exp. Cell Res.* 232: 439–442.
45. Kumagai, K., K. Tabu, F. Sasaki, Y. Takami, Y. Morinaga, S. Mawatari, S. Hashimoto, S. Tanoue, S. Kanmura, T. Tamai, et al. 2015. Glycoprotein nonmetastatic melanoma B (Gpnmb)-positive macrophages contribute to the balance between fibrosis and fibrolysis during the repair of acute liver injury in mice. *PLoS One* 10: e0143413.
46. Sasaki, F., K. Kumagai, H. Uto, Y. Takami, T. Kure, K. Tabu, Y. Nasu, S. Hashimoto, S. Kanmura, M. Numata, et al. 2015. Expression of glycoprotein nonmetastatic melanoma protein B in macrophages infiltrating injured mucosa is associated with the severity of experimental colitis in mice. *Mol. Med. Rep.* 12: 7503–7511.
47. Ripoll, V. M., K. M. Irvine, T. Ravasi, M. J. Sweet, and D. A. Hume. 2007. Gpnmb is induced in macrophages by IFN-gamma and lipopolysaccharide and acts as a feedback regulator of proinflammatory responses. *J. Immunol.* 178: 6557–6566.
48. Li, X. F., C. Chen, D. M. Xiang, L. Qu, W. Sun, X. Y. Lu, T. F. Zhou, S. Z. Chen, B. F. Ning, Z. Cheng, et al. 2017. Chronic inflammation-elicited liver progenitor cell conversion to liver cancer stem cell with clinical significance. *Hepatology* 66: 1934–1951.
49. Borriello, L., R. Nakata, M. A. Sheard, G. E. Fernandez, R. Sposto, J. Malvar, L. Blavier, H. Shimada, S. Asgharzadeh, R. C. Seeger, and Y. A. DeClerck. 2017. Cancer-associated fibroblasts share characteristics and protumorigenic activity with mesenchymal stromal cells. *Cancer Res.* 77: 5142–5157.
50. Hazan-Halevy, I., D. Harris, Z. Liu, J. Liu, P. Li, X. Chen, S. Shanker, A. Ferrajoli, M. J. Keating, and Z. Estrov. 2010. STAT3 is constitutively phosphorylated on serine 727 residues, binds DNA, and activates transcription in CLL cells. *Blood* 115: 2852–2863.
51. Lai, R., G. Z. Rassidakis, L. J. Medeiros, V. Leventaki, M. Keating, and T. J. McDonnell. 2003. Expression of STAT3 and its phosphorylated forms in mantle cell lymphoma cell lines and tumours. *J. Pathol.* 199: 84–89.
52. Bromberg, J. 2002. Stat proteins and oncogenesis. *J. Clin. Invest.* 109: 1139–1142.
53. Yu, H., and R. Jove. 2004. The STATs of cancer–new molecular targets come of age. *Nat. Rev. Cancer* 4: 97–105.
54. Fang, L., J. Hodge, F. Saaoud, J. Wang, S. Iwanowycz, Y. Wang, Y. Hui, T. D. Evans, B. Razani, and D. Fan. 2017. Transcriptional factor EB regulates macrophage polarization in the tumor microenvironment. *OncoImmunology* 6: e1312042.
55. Letterio, J. J., and A. B. Roberts. 1998. Regulation of immune responses by TGF-beta. *Annu. Rev. Immunol.* 16: 137–161.
56. Chithra, P. K., A. Jayalekshmy, and A. Helen. 2017. Petroleum ether extract of Njavara rice (Oryza sativa) bran upregulates the JAK2-STAT3-mediated anti-inflammatory profile in macrophages and aortic endothelial cells promoting regression of atherosclerosis. *Biochem. Cell Biol.* 95: 652–662.
57. Salmiheimo, A., H. Mustonen, S. Vainionpää, Z. Shen, E. Kemppainen, P. Puolakkainen, and H. Seppänen. 2017. Tumour-associated macrophages activate migration and STAT3 in pancreatic ductal adenocarcinoma cells in co-cultures. *Pancreatology* 17: 635–641.
58. Titos, E., B. Rius, C. López-Vicario, J. Alcaraz-Quiles, V. García-Alonso, A. Lopategi, J. Dalli, J. J. Lozano, V. Arroyo, S. Delgado, et al. 2016. Signaling

and immunoresolving actions of resolvin D1 in inflamed human visceral adipose tissue. *J. Immunol.* 197: 3360–3370.
59. Fallowfield, J. A., A. L. Hayden, V. K. Snowdon, R. L. Aucott, B. M. Stutchfield, D. J. Mole, A. Pellicoro, T. T. Gordon-Walker, A. Henke, J. Schrader, et al. 2014. Relaxin modulates human and rat hepatic myofibroblast function and ameliorates portal hypertension in vivo. *Hepatology* 59: 1492–1504.
60. Hucke, S., M. Eschborn, M. Liebmann, M. Herold, N. Freise, A. Engbers, P. Ehling, S. G. Meuth, J. Roth, T. Kuhlmann, et al. 2016. Sodium chloride promotes pro-inflammatory macrophage polarization thereby aggravating CNS autoimmunity. *J. Autoimmun.* 67: 90–101.
61. Han, K. H., R. Gonzalez-Quintial, Y. Peng, R. Baccala, A. N. Theofilopoulos, and R. A. Lerner. 2016. An agonist antibody that blocks autoimmunity by inducing anti-inflammatory macrophages. *FASEB J.* 30: 738–747.
62. Stutchfield, B. M., D. J. Antoine, A. C. Mackinnon, D. J. Gow, C. C. Bain, C. A. Hawley, M. J. Hughes, B. Francis, D. Wojtacha, T. Y. Man, et al. 2015. CSF1 restores innate immunity after liver injury in mice and serum levels indicate outcomes of patients with acute liver failure. *Gastroenterology* 149: 1896–1909.e14.
63. Wan, S., E. Zhao, I. Kryczek, L. Vatan, A. Sadovskaya, G. Ludema, D. M. Simeone, W. Zou, and T. H. Welling. 2014. Tumor-associated macrophages produce interleukin 6 and signal via STAT3 to promote expansion of human hepatocellular carcinoma stem cells. *Gastroenterology* 147: 1393–1404.
64. Wang, Q., F. Cheng, T. T. Ma, H. Y. Xiong, Z. W. Li, C. L. Xie, C. Y. Liu, and Z. G. Tu. 2016. Interleukin-12 inhibits the hepatocellular carcinoma growth by inducing macrophage polarization to the M1-like phenotype through downregulation of Stat-3. *Mol. Cell. Biochem.* 415: 157–168.
65. Casella, G., L. Garzetti, A. T. Gatta, A. Finardi, C. Maiorino, F. Ruffini, G. Martino, L. Muzio, and R. Furlan. 2016. IL4 induces IL6-producing M2 macrophages associated to inhibition of neuroinflammation in vitro and in vivo. *J. Neuroinflammation* 13: 139.